

Implementation of a Smeared Crack Band Model in a Micromechanics Framework

*Evan J. Pineda and Brett A. Bednarczyk
Glenn Research Center, Cleveland, Ohio*

*Anthony M. Waas
University of Michigan, Ann Arbor, Michigan*

*Steven M. Arnold
Glenn Research Center, Cleveland, Ohio*

NASA STI Program . . . in Profile

Since its founding, NASA has been dedicated to the advancement of aeronautics and space science. The NASA Scientific and Technical Information (STI) program plays a key part in helping NASA maintain this important role.

The NASA STI Program operates under the auspices of the Agency Chief Information Officer. It collects, organizes, provides for archiving, and disseminates NASA's STI. The NASA STI program provides access to the NASA Aeronautics and Space Database and its public interface, the NASA Technical Reports Server, thus providing one of the largest collections of aeronautical and space science STI in the world. Results are published in both non-NASA channels and by NASA in the NASA STI Report Series, which includes the following report types:

- **TECHNICAL PUBLICATION.** Reports of completed research or a major significant phase of research that present the results of NASA programs and include extensive data or theoretical analysis. Includes compilations of significant scientific and technical data and information deemed to be of continuing reference value. NASA counterpart of peer-reviewed formal professional papers but has less stringent limitations on manuscript length and extent of graphic presentations.
- **TECHNICAL MEMORANDUM.** Scientific and technical findings that are preliminary or of specialized interest, e.g., quick release reports, working papers, and bibliographies that contain minimal annotation. Does not contain extensive analysis.
- **CONTRACTOR REPORT.** Scientific and technical findings by NASA-sponsored contractors and grantees.

- **CONFERENCE PUBLICATION.** Collected papers from scientific and technical conferences, symposia, seminars, or other meetings sponsored or cosponsored by NASA.
- **SPECIAL PUBLICATION.** Scientific, technical, or historical information from NASA programs, projects, and missions, often concerned with subjects having substantial public interest.
- **TECHNICAL TRANSLATION.** English-language translations of foreign scientific and technical material pertinent to NASA's mission.

Specialized services also include creating custom thesauri, building customized databases, organizing and publishing research results.

For more information about the NASA STI program, see the following:

- Access the NASA STI program home page at <http://www.sti.nasa.gov>
- E-mail your question via the Internet to help@sti.nasa.gov
- Fax your question to the NASA STI Help Desk at 443-757-5803
- Telephone the NASA STI Help Desk at 443-757-5802
- Write to:
NASA Center for AeroSpace Information (CASI)
7115 Standard Drive
Hanover, MD 21076-1320



Implementation of a Smearred Crack Band Model in a Micromechanics Framework

*Evan J. Pineda and Brett A. Bednarczyk
Glenn Research Center, Cleveland, Ohio*

*Anthony M. Waas
University of Michigan, Ann Arbor, Michigan*

*Steven M. Arnold
Glenn Research Center, Cleveland, Ohio*

National Aeronautics and
Space Administration

Glenn Research Center
Cleveland, Ohio 44135

Trade names and trademarks are used in this report for identification only. Their usage does not constitute an official endorsement, either expressed or implied, by the National Aeronautics and Space Administration.

Level of Review: This material has been technically reviewed by technical management.

Available from

NASA Center for Aerospace Information
7115 Standard Drive
Hanover, MD 21076-1320

National Technical Information Service
5301 Shawnee Road
Alexandria, VA 22312

Available electronically at <http://www.sti.nasa.gov>

Implementation of a Smeared Crack Band Model in a Micromechanics Framework

Evan J. Pineda and Brett A. Bednarczyk
National Aeronautics and Space Administration
Glenn Research Center
Cleveland, Ohio 44135

Anthony M. Waas
University of Michigan
Ann Arbor, Michigan 48109

Steven M. Arnold
National Aeronautics and Space Administration
Glenn Research Center
Cleveland, Ohio 44135

1 Introduction

Micromechanics techniques can be employed to model the individual constituents within the composite. Typically, a repeating unit cell (RUC) in the composite microstructure is identified and analysis is performed on that RUC assuming periodic boundary conditions. The response of a point in a continuum is determined assuming an infinite array of the RUCs. However, representative volume element (RVE) methodologies exist which incorporate applying non-periodic boundary conditions to a subvolume that accurately represents the composite microstructure. The RVE is meant to represent the actual microstructure of the continuum, and the size of the features of the microstructure is preserved. Micromechanics can be utilized to provide the homogenized composite stiffness, or they can be used to model damage and failure within the constituents. If utilized for the latter, the global mechanisms can arise through the natural evolution and interaction of the mechanisms in the constituents in the micromechanics model. Numerous micromechanical frameworks exist that encompass analytical, semi-analytical, and numerical techniques. An expansive review of many micromechanics theories is given in Ref. [Aboudi *et al.* (2012)]. In this work a discretization insensitive continuum damage model (CDM) is implemented within the high-fidelity generalized method of cells (HFGMC) to model transverse cracking and compressive shear banding in a unidirectional fiber-reinforced polymer matrix composite (PMC).

The method of cells (MOC) developed by *Aboudi* (1991) discretized a rectangular composite RUC into four subvolumes, called subcells. One of the subcells was occupied by the fiber material and the rest were occupied by the matrix. Linear displacement fields were assumed in each of the subcells. Displacement and traction continuity conditions were enforced, in an average integral sense, at the subcell interfaces, along with periodic boundary conditions at the RUC boundaries to derive a set of equations that would yield a strain concentration matrix that could, in turn,

be used to obtain the local subcell strains from the applied fields. Following determination of the subcell strains, the subcell stress are readily calculated using the local constitutive laws, and volume averaging can be used to obtain the homogenized thermomechanical properties of the composite. MOC was later extended to the generalized method of cells (GMC) by *Paley and Aboudi* (1992) which accommodated any number of subcells and constituents in two-periodic directions. *Aboudi* (1995) adapted the formulation to accommodate triply-periodic materials. Finally, *Aboudi et al.* (2001) developed HFGMC which utilized second order displacement field approximations in the subcells, rather than linear. *Haj-Ali and Aboudi* (2009) showed the local elastic field accuracy produced by HFGMC corresponded very well to FEM; whereas, *Aboudi et al.* (2003) compared the accuracy of the fields in inelastic phases to composite cylinder assemblage (CCA). *Bednarczyk et al.* (2004) utilized HFGMC to model fiber-matrix debonding in metal matrix composites (MMCs), and *Bednarczyk et al.* (2010) implemented a multi-axial damage model in HFGMC. Reformulations, of GMC and HFGMC, which reduced the total number of unknowns in the problem were introduced by *Pindera and Bednarczyk* (1997) and *Aboudi et al.* (2012), respectively.

The generality of the GMC and HFGMC formulations admit any constitutive behavior at the subcell level. However if the response of the subcell material exhibits post-peak strain softening the tangent stiffness tensor of the subcell loses positive definiteness. This leads to pathologically mesh dependent behavior.

Bažant and Oh (1983) developed the smeared crack band approach which introduced a characteristic element length into the post-peak softening damage evolution formulation. The tangent slope of the softening stress-strain curve was scaled by the characteristic length to ensure that total strain energy release rate (SERR) upon complete failure (i.e. zero stress) is always equal to the prescribed fracture toughness, regardless of the element size. In the original formulation, the band was always oriented perpendicular to the direction of maximum principal stress; thus, the crack

band always advanced under pure mode I. *de Borst and Nauta* (1985); *Rots and de Borst* (1987) later reformulated the model to incorporate a fixed crack band that evolved under mixed-mode conditions. Both formulations employ linear degradation schemes. Later, *Camanho et al.* (2007) incorporated more sophisticated initiation criteria to predict the onset of mixed-mode crack bands. All of these smeared crack formulations assume linear elastic behavior up to the initiation of the crack band, followed by immediate post-peak strain softening. However, *Spencer* (2002) coupled pre-peak plasticity with crack band post-peak strain softening in modeling failure of concrete.

A variation of the crack band model developed by *Bazant and Oh* (1983) for concrete structures is implemented here within the HFGMC micromechanics framework to model mesh objective failure of continuous fiber-reinforced polymer matrix composites. The focus is restricted to the microscale to evaluate the capabilities of the smeared crack band model to predict progressive failure evolution within a composite microstructure. Thus, a detailed, multiple-fiber RUC is chosen demonstrate these capabilities. HFGMC is utilized as the micromechanics platform because the level of fidelity required to accurately model failure evolution in a complex microstructure is not provided by GMC.

In Section 2 the formulation for HFGMC is given, followed by the implementation of the smeared crack band model in Section 3. Two scenarios are considered to determine the mode in which the cracks within the crack band grow. If the principal stress that has the highest magnitude is tensile, it is assumed that it is more energetically favorable for the crack band to form perpendicular to the maximum principal stress and for the cracks within the band to advance under mode I conditions. Conversely, if the the magnitude of a compressive principal stress is higher than the other principal stresses, the cracks within the crack band evolve under mode II conditions (due to internal, Mohr-Coulomb friction) and are oriented with the plane of maximum shear

stress. In Section 4 the objectivity of the post-peak softening behavior of the model with respect to the subcell mesh is shown. An example is presented in Section 5 that consists of an RUC composed of 13, randomly placed fibers that is subjected to transverse tension and compression. The model is verified against experimental data in Section 6.

The motivation behind the following developments is to arrive at a failure methodology that is capable of accurately capturing localization in a multiscale model without any spurious dependencies. This paper is intended to present results that verify a model for such an application. In Section 7 a multiscale methodology is introduced that ensures mesh objectivity and addresses the issues presented by *Bažant* (2007).

2 The High-Fidelity Generalized Method of Cells

HFGMC, first introduced by *Aboudi et al.* (1999) resolves some of the shortcomings of the original GMC. The biggest of which is the lack of normal-shear coupling in GMC which results from the enforcement of displacement and traction continuity in an average, integral sense and a linear approximation of the displacement fields in each subcell. HFGMC employs quadratic displacement approximations. However, this requires more equations than can be produced using displacement and traction continuity. Thus, the zeroth, first, and second moments of equilibrium are used to solve the problem.

It is assumed that a composite microstructure can be represented as a collection of triply periodic RUCs containing a general number of constituents, as shown in Figure 1. The RUC is then discretized into $N_\alpha \times N_\beta \times N_\gamma$ rectangular, prismatic subcells, as exhibited in Figure 2. Each of these subcells are occupied by one of the constituents in the composite. The number of subcells and the materials occupying each subcell are completely general. For a two-phase fibrous composite any desired micro-architecture

can be represented by occupying each subcell with either a matrix or fiber constituent. Since the microstructure does not vary along the axial, fiber-direction, a unidirectional composite can be modeled using a doubly-periodic RUC (Figure 3), where the x_2 - x_3 plane is discretized. Herein, doubly-periodic formulations of HFGMC [Aboudi *et al.* (1999)] will be employed; the reader is referred to Ref. [Aboudi *et al.* (2012)] for the fully 3D formulations, as well as a more efficient reformulation.

2.1 Governing Equations

The 3D equilibrium equations for subcell $\beta\gamma$ (see Figure 4) in a doubly-periodic RUC (Figure 3) are given by

$$\partial_1 \sigma_{1i}^{(\beta\gamma)} + \partial_2 \sigma_{2i}^{(\beta\gamma)} + \partial_3 \sigma_{3i}^{(\beta\gamma)} = 0 \quad (1)$$

Since there is no variation in the x_1 -direction for a doubly-periodic material, $\partial_1 = \partial/\partial x_1 = 0$. Therefore Equation (1) becomes

$$\partial_2 \sigma_{2i}^{(\beta\gamma)} + \partial_3 \sigma_{3i}^{(\beta\gamma)} = 0 \quad (2)$$

Averaging Equation (2) over the volume of the subcell yields

$$J_{2i(00)}^{(\beta\gamma)} + K_{3i(00)}^{(\beta\gamma)} = 0 \quad (3)$$

where

$$J_{2i(00)}^{(\beta\gamma)} = \frac{1}{h_\beta} \left[{}^{(2)}t_i^{+(\beta\gamma)} - {}^{(2)}t_i^{-(\beta\gamma)} \right] \quad (4)$$

and

$$K_{3i(00)}^{(\beta\gamma)} = \frac{1}{l_\gamma} \left[{}^{(3)}t_i^{+(\beta\gamma)} - {}^{(3)}t_i^{-(\beta\gamma)} \right] \quad (5)$$

The surface tractions are given by

$${}^{(2)}t_i^{\pm(\beta\gamma)} = \frac{1}{l_\gamma} \int_{-l_\gamma/2}^{l_\gamma/2} \sigma_{2i}^{(\beta\gamma)} \left(\bar{x}_2^{(\beta)} = \pm \frac{h_\beta}{2} \right) d\bar{x}_3^{(\gamma)} \quad (6)$$

$${}^{(3)}t_i^{\pm(\beta\gamma)} = \frac{1}{h_\beta} \int_{-h_\beta/2}^{h_\beta/2} \sigma_{3i}^{(\beta\gamma)} \left(\bar{x}_3^{(\gamma)} = \pm \frac{l_\gamma}{2} \right) d\bar{x}_2^{(\beta)} \quad (7)$$

where “(2)” and “(3)” are superscripts that indicate the applicable normal direction to the subcell surface and “ \pm ” indicates the sign of the normal. Similarly, the first moment of equilibrium can also be averaged over the subcell volume resulting in

$$J_{2i(10)}^{(\beta\gamma)} - S_{2i(00)}^{(\beta\gamma)} = 0 \quad (8)$$

and

$$K_{3i(01)}^{(\beta\gamma)} - S_{3i(00)}^{(\beta\gamma)} = 0 \quad (9)$$

where $S_{ij(mn)}^{(\beta\gamma)}$ is an average stress quantity, and

$$J_{2i(10)}^{(\beta\gamma)} = \frac{1}{2} \left[{}^{(2)}t_i^{+(\beta\gamma)} + {}^{(2)}t_i^{-(\beta\gamma)} \right] \quad (10)$$

$$K_{3i(01)}^{(\beta\gamma)} = \frac{1}{2} \left[{}^{(3)}t_i^{+(\beta\gamma)} + {}^{(3)}t_i^{-(\beta\gamma)} \right] \quad (11)$$

$$S_{ij(mn)}^{(\beta\gamma)} = \frac{1}{h_\beta l_\gamma} \int_{-h_\beta/2}^{h_\beta/2} \int_{-l_\gamma/2}^{l_\gamma/2} \sigma_{ij}^{(\beta\gamma)} (\bar{x}_2^{(\beta)})^m (\bar{x}_3^{(\gamma)})^n d\bar{x}_2^{(\beta)} d\bar{x}_3^{(\gamma)} \quad (12)$$

Finally, the second moment of equilibrium can be averaged over the subcell volume, then utilizing integration by parts leads to

$$\frac{h_\beta^2}{4} J_{2i(00)}^{(\beta\gamma)} + \frac{h_\beta^2}{12} K_{3i(00)}^{(\beta\gamma)} - 2S_{2i(10)}^{(\beta\gamma)} = 0 \quad (13)$$

and

$$\frac{l_\gamma^2}{12} J_{2i(00)}^{(\beta\gamma)} + \frac{l_\gamma^2}{4} K_{3i(00)}^{(\beta\gamma)} - 2S_{3i(01)}^{(\beta\gamma)} = 0 \quad (14)$$

Substituting Equations (13) and (14) into Equation (3) gives

$$J_{2i(00)}^{(\beta\gamma)} = \frac{12}{h_\beta^2} S_{2i(10)}^{(\beta\gamma)} \quad (15)$$

$$K_{3i(00)}^{(\beta\gamma)} = \frac{12}{l_\gamma^2} S_{3i(01)}^{(\beta\gamma)} \quad (16)$$

Utilizing Equations (15) and (16) in Equation (14):

$$\frac{1}{h_\beta^2} S_{2i(10)}^{(\beta\gamma)} + \frac{1}{l_\gamma^2} S_{3i(01)}^{(\beta\gamma)} = 0 \quad (17)$$

Equation (17) represents the average form, in HFGMC, of the equilibrium equations, Equation (2), of subcell $\beta\gamma$ within a doubly-periodic composite RUC.

2.2 Second Order Displacement Approximation

Contrary to GMC, HFGMC employs a quadratic expansion of the subcell displacements

$$u_i^{(\beta\gamma)} = \bar{\epsilon}_{ij} x_j + W_{i(00)}^{(\beta\gamma)} + \bar{x}_2^{(\beta)} W_{i(10)}^{(\beta\gamma)} + \bar{x}_3^{(\gamma)} W_{i(01)}^{(\beta\gamma)} + \frac{1}{2} \left(3\bar{x}_2^{(\beta)^2} - \frac{h_\beta^2}{4} \right) W_{i(20)}^{(\beta\gamma)} + \frac{1}{2} \left(3\bar{x}_3^{(\gamma)^2} - \frac{l_\gamma^2}{4} \right) W_{i(02)}^{(\beta\gamma)} \quad (18)$$

where $\bar{\epsilon}_{ij}$ are, as in GMC, the average global strain components, and $W_{i(mn)}^{(\beta\gamma)}$ are microvariables describing the spatial variation of the displacement field and are determined by enforcing interfacial and periodic conditions.

2.3 Constitutive Relations

The local strains in subcell $\beta\gamma$ are related to the global strains and local displacement fields through

$$\epsilon_{ij}^{(\beta\gamma)} = \bar{\epsilon}_{ij} + \frac{1}{2} \left(\partial_i u_j^{(\beta\gamma)} + \partial_j u_i^{(\beta\gamma)} \right) \quad (19)$$

Employing the local constitutive law,

$$\sigma_{ij}^{(\beta\gamma)} = C_{ijkl}^{(\beta\gamma)} \epsilon_{kl}^{(\beta\gamma)} \quad (20)$$

ignoring plastic and thermal effects (for HFGMC formulation with plasticity and thermal strains please see Ref. [Aboudi *et al.* (2003)]) in Equation (12) along with Equations (18) and (19), the relationship between zeroth order stress components and the microvariables is determined to be:

$$\begin{aligned} S_{11(00)}^{(\beta\gamma)} &= C_{11}^{(\beta\gamma)} \bar{\epsilon}_{11} + C_{12}^{(\beta\gamma)} \left(W_{2(10)}^{(\beta\gamma)} + \bar{\epsilon}_{22} \right) + C_{13}^{(\beta\gamma)} \left(W_{3(01)}^{(\beta\gamma)} + \bar{\epsilon}_{33} \right) \\ &+ C_{14}^{(\beta\gamma)} \left(W_{2(01)}^{(\beta\gamma)} + W_{3(10)}^{(\beta\gamma)} + 2\bar{\epsilon}_{23} \right) + C_{15}^{(\beta\gamma)} \left(W_{1(01)}^{(\beta\gamma)} + 2\bar{\epsilon}_{13} \right) \\ &+ C_{16}^{(\beta\gamma)} \left(W_{1(10)}^{(\beta\gamma)} + 2\bar{\epsilon}_{12} \right) \end{aligned} \quad (21)$$

$$\begin{aligned} S_{22(00)}^{(\beta\gamma)} &= C_{12}^{(\beta\gamma)} \bar{\epsilon}_{11} + C_{22}^{(\beta\gamma)} \left(W_{2(10)}^{(\beta\gamma)} + \bar{\epsilon}_{22} \right) + C_{23}^{(\beta\gamma)} \left(W_{3(01)}^{(\beta\gamma)} + \bar{\epsilon}_{33} \right) \\ &+ C_{24}^{(\beta\gamma)} \left(W_{2(01)}^{(\beta\gamma)} + W_{3(10)}^{(\beta\gamma)} + 2\bar{\epsilon}_{23} \right) + C_{25}^{(\beta\gamma)} \left(W_{1(01)}^{(\beta\gamma)} + 2\bar{\epsilon}_{13} \right) \\ &+ C_{26}^{(\beta\gamma)} \left(W_{1(10)}^{(\beta\gamma)} + 2\bar{\epsilon}_{12} \right) \end{aligned} \quad (22)$$

$$\begin{aligned} S_{33(00)}^{(\beta\gamma)} &= C_{13}^{(\beta\gamma)} \bar{\epsilon}_{11} + C_{23}^{(\beta\gamma)} \left(W_{2(10)}^{(\beta\gamma)} + \bar{\epsilon}_{22} \right) + C_{33}^{(\beta\gamma)} \left(W_{3(01)}^{(\beta\gamma)} + \bar{\epsilon}_{33} \right) \\ &+ C_{34}^{(\beta\gamma)} \left(W_{2(01)}^{(\beta\gamma)} + W_{3(10)}^{(\beta\gamma)} + 2\bar{\epsilon}_{23} \right) + C_{35}^{(\beta\gamma)} \left(W_{1(01)}^{(\beta\gamma)} + 2\bar{\epsilon}_{13} \right) \\ &+ C_{36}^{(\beta\gamma)} \left(W_{1(10)}^{(\beta\gamma)} + 2\bar{\epsilon}_{12} \right) \end{aligned} \quad (23)$$

$$\begin{aligned} S_{44(00)}^{(\beta\gamma)} &= C_{14}^{(\beta\gamma)} \bar{\epsilon}_{11} + C_{24}^{(\beta\gamma)} \left(W_{2(10)}^{(\beta\gamma)} + \bar{\epsilon}_{22} \right) + C_{34}^{(\beta\gamma)} \left(W_{3(01)}^{(\beta\gamma)} + \bar{\epsilon}_{33} \right) \\ &+ C_{44}^{(\beta\gamma)} \left(W_{2(01)}^{(\beta\gamma)} + W_{3(10)}^{(\beta\gamma)} + 2\bar{\epsilon}_{23} \right) + C_{45}^{(\beta\gamma)} \left(W_{1(01)}^{(\beta\gamma)} + 2\bar{\epsilon}_{13} \right) \\ &+ C_{46}^{(\beta\gamma)} \left(W_{1(10)}^{(\beta\gamma)} + 2\bar{\epsilon}_{12} \right) \end{aligned} \quad (24)$$

$$\begin{aligned}
S_{55(00)}^{(\beta\gamma)} &= C_{15}^{(\beta\gamma)} \bar{\epsilon}_{11} + C_{25}^{(\beta\gamma)} \left(W_{2(10)}^{(\beta\gamma)} + \bar{\epsilon}_{22} \right) + C_{35}^{(\beta\gamma)} \left(W_{3(01)}^{(\beta\gamma)} + \bar{\epsilon}_{33} \right) \\
&+ C_{45}^{(\beta\gamma)} \left(W_{2(01)}^{(\beta\gamma)} + W_{3(10)}^{(\beta\gamma)} + 2\bar{\epsilon}_{23} \right) + C_{55}^{(\beta\gamma)} \left(W_{1(01)}^{(\beta\gamma)} + 2\bar{\epsilon}_{13} \right) \\
&+ C_{56}^{(\beta\gamma)} \left(W_{1(10)}^{(\beta\gamma)} + 2\bar{\epsilon}_{12} \right)
\end{aligned} \tag{25}$$

$$\begin{aligned}
S_{66(00)}^{(\beta\gamma)} &= C_{16}^{(\beta\gamma)} \bar{\epsilon}_{11} + C_{26}^{(\beta\gamma)} \left(W_{2(10)}^{(\beta\gamma)} + \bar{\epsilon}_{22} \right) + C_{36}^{(\beta\gamma)} \left(W_{3(01)}^{(\beta\gamma)} + \bar{\epsilon}_{33} \right) \\
&+ C_{46}^{(\beta\gamma)} \left(W_{2(01)}^{(\beta\gamma)} + W_{3(10)}^{(\beta\gamma)} + 2\bar{\epsilon}_{23} \right) + C_{56}^{(\beta\gamma)} \left(W_{1(01)}^{(\beta\gamma)} + 2\bar{\epsilon}_{13} \right) \\
&+ C_{66}^{(\beta\gamma)} \left(W_{1(10)}^{(\beta\gamma)} + 2\bar{\epsilon}_{12} \right)
\end{aligned} \tag{26}$$

where the contracted notation for the stiffness tensor components $C_{ij}^{(\beta\gamma)}$ is used. Similarly the first stress moments are

$$S_{11(10)}^{(\beta\gamma)} = \frac{h_\beta^2}{4} \left[C_{12}^{(\beta\gamma)} W_{2(20)}^{(\beta\gamma)} + C_{14}^{(\beta\gamma)} W_{3(20)}^{(\beta\gamma)} + C_{16}^{(\beta\gamma)} W_{1(20)}^{(\beta\gamma)} \right] \tag{27}$$

$$S_{11(01)}^{(\beta\gamma)} = \frac{l_\gamma^2}{4} \left[C_{13}^{(\beta\gamma)} W_{3(02)}^{(\beta\gamma)} + C_{14}^{(\beta\gamma)} W_{2(02)}^{(\beta\gamma)} + C_{15}^{(\beta\gamma)} W_{1(02)}^{(\beta\gamma)} \right] \tag{28}$$

$$S_{22(10)}^{(\beta\gamma)} = \frac{h_\beta^2}{4} \left[C_{22}^{(\beta\gamma)} W_{2(20)}^{(\beta\gamma)} + C_{24}^{(\beta\gamma)} W_{3(20)}^{(\beta\gamma)} + C_{26}^{(\beta\gamma)} W_{1(20)}^{(\beta\gamma)} \right] \tag{29}$$

$$S_{22(01)}^{(\beta\gamma)} = \frac{l_\gamma^2}{4} \left[C_{23}^{(\beta\gamma)} W_{3(02)}^{(\beta\gamma)} + C_{24}^{(\beta\gamma)} W_{2(02)}^{(\beta\gamma)} + C_{25}^{(\beta\gamma)} W_{1(02)}^{(\beta\gamma)} \right] \tag{30}$$

$$S_{33(10)}^{(\beta\gamma)} = \frac{h_\beta^2}{4} \left[C_{23}^{(\beta\gamma)} W_{2(20)}^{(\beta\gamma)} + C_{34}^{(\beta\gamma)} W_{3(20)}^{(\beta\gamma)} + C_{36}^{(\beta\gamma)} W_{1(20)}^{(\beta\gamma)} \right] \tag{31}$$

$$S_{33(01)}^{(\beta\gamma)} = \frac{l_\gamma^2}{4} \left[C_{33}^{(\beta\gamma)} W_{3(02)}^{(\beta\gamma)} + C_{34}^{(\beta\gamma)} W_{2(02)}^{(\beta\gamma)} + C_{35}^{(\beta\gamma)} W_{1(02)}^{(\beta\gamma)} \right] \tag{32}$$

$$S_{44(10)}^{(\beta\gamma)} = \frac{h_\beta^2}{4} \left[C_{24}^{(\beta\gamma)} W_{2(20)}^{(\beta\gamma)} + C_{44}^{(\beta\gamma)} W_{3(20)}^{(\beta\gamma)} + C_{46}^{(\beta\gamma)} W_{1(20)}^{(\beta\gamma)} \right] \tag{33}$$

$$S_{55(01)}^{(\beta\gamma)} = \frac{l_\gamma^2}{4} \left[C_{35}^{(\beta\gamma)} W_{3(02)}^{(\beta\gamma)} + C_{45}^{(\beta\gamma)} W_{2(02)}^{(\beta\gamma)} + C_{55}^{(\beta\gamma)} W_{1(02)}^{(\beta\gamma)} \right] \tag{34}$$

$$S_{66(10)}^{(\beta\gamma)} = \frac{h_\beta^2}{4} \left[C_{26}^{(\beta\gamma)} W_{2(20)}^{(\beta\gamma)} + C_{46}^{(\beta\gamma)} W_{3(20)}^{(\beta\gamma)} + C_{66}^{(\beta\gamma)} W_{1(20)}^{(\beta\gamma)} \right] \tag{35}$$

$$S_{66(01)}^{(\beta\gamma)} = \frac{l_\gamma^2}{4} \left[C_{36}^{(\beta\gamma)} W_{3(02)}^{(\beta\gamma)} + C_{46}^{(\beta\gamma)} W_{2(02)}^{(\beta\gamma)} + C_{56}^{(\beta\gamma)} W_{1(02)}^{(\beta\gamma)} \right] \tag{36}$$

2.4 Displacement Continuity

The unknown microvariables (the volume-averaged displacement vector $W_{i(00)}^{(\beta\gamma)}$ and the higher order terms $W_{i(mn)}^{(\beta\gamma)}$) can be calculated from the governing equation, Equation (17), subcell interfacial continuity conditions, and periodicity conditions.

The periodic boundary conditions for an RUC are given by

$$u_i|_{x_2=0} = u_i|_{x_2=H} \quad (37)$$

$$\sigma_{2i}|_{x_2=0} = \sigma_{2i}|_{x_2=H} \quad (38)$$

$$u_i|_{x_3=0} = u_i|_{x_3=L} \quad (39)$$

$$\sigma_{3i}|_{x_3=0} = \sigma_{3i}|_{x_3=L} \quad (40)$$

The displacement continuity conditions are enforced, as in GMC, in an average (integral) sense, yielding:

$$\int_{-l_\gamma/2}^{l_\gamma/2} \left[u_i^{(1\gamma)} \Big|_{\bar{x}_2^{(1)} = -h_1/2} \right] d\bar{x}_3^{(\gamma)} = \int_{-l_\gamma/2}^{l_\gamma/2} \left[u_i^{(N_\beta\gamma)} \Big|_{\bar{x}_2^{(N_\beta)} = h_{N_\beta}/2} \right] d\bar{x}_3^{(\gamma)}, \quad \gamma = 1, \dots, N_\gamma \quad (41)$$

$$\int_{-h_\beta/2}^{h_\beta/2} \left[u_i^{(\beta 1)} \Big|_{\bar{x}_3^{(1)} = -l_1/2} \right] d\bar{x}_2^{(\beta)} = \int_{-h_\beta/2}^{h_\beta/2} \left[u_i^{(\beta N_\gamma)} \Big|_{\bar{x}_3^{(N_\gamma)} = l_{N_\gamma}/2} \right] d\bar{x}_2^{(\beta)}, \quad \beta = 1, \dots, N_\beta \quad (42)$$

Using the definition of the subcell displacements, Equation (18), in the average displacement continuity conditions, Equations (41) and (42), gives:

$$W_{i(00)}^{(1\gamma)} - \frac{h_1}{2} W_{i(10)}^{(1\gamma)} - \frac{h_1^2}{4} W_{i(20)}^{(1\gamma)} = W_{i(00)}^{(N_\beta\gamma)} - \frac{h_{N_\beta}}{2} W_{i(10)}^{(N_\beta\gamma)} - \frac{h_{N_\beta}^2}{4} W_{i(20)}^{(N_\beta\gamma)}, \quad \gamma = 1, \dots, N_\gamma \quad (43)$$

$$W_{i(00)}^{(\beta 1)} - \frac{l_1}{2} W_{i(01)}^{(\beta 1)} - \frac{l_1^2}{4} W_{i(02)}^{(\beta 1)} = W_{i(00)}^{(\beta N_\gamma)} - \frac{l_{N_\gamma}}{2} W_{i(01)}^{(\beta N_\gamma)} - \frac{l_{N_\gamma}^2}{4} W_{i(02)}^{(\beta N_\gamma)}, \quad \beta = 1, \dots, N_\beta \quad (44)$$

Equations (43) and (44) represent the displacement continuity conditions necessary

to enforce periodicity of the RUC. Similar relations can be derived to enforce displacement continuity across adjacent subcell boundaries,

$$W_{i(00)}^{(\beta\gamma)} + \frac{h_\beta}{2} W_{i(10)}^{(\beta\gamma)} + \frac{h_\beta^2}{4} W_{i(20)}^{(\beta\gamma)} = W_{i(00)}^{(\beta+1\gamma)} + \frac{h_{\beta+1}}{2} W_{i(10)}^{(\beta+1\gamma)} + \frac{h_{\beta+1}^2}{4} W_{i(20)}^{(\beta+1\gamma)}, \quad (45)$$

$$\beta = 1, \dots, N_\beta - 1, \quad \gamma = 1, \dots, N_\gamma$$

$$W_{i(00)}^{(\beta\gamma)} + \frac{l_\gamma}{2} W_{i(01)}^{(\beta\gamma)} + \frac{l_\gamma^2}{4} W_{i(02)}^{(\beta\gamma)} = W_{i(00)}^{(\beta\gamma+1)} + \frac{l_{\gamma+1}}{2} W_{i(01)}^{(\beta\gamma+1)} + \frac{l_{\gamma+1}^2}{4} W_{i(02)}^{(\beta\gamma+1)}, \quad (46)$$

$$\beta = 1, \dots, N_\beta, \quad \gamma = 1, \dots, N_\gamma - 1$$

Note that Equations (43)-(44) can be relaxed to incorporate the effects of local, interfacial debonding [Bednarczyk *et al.* (2004)].

2.5 Traction Continuity

Similarly using Equations (6) and (7), the average implementation of the stress periodicity conditions (Equations (38) and (40)) is

$${}^{(2)}t_i^{+(1\gamma)} = {}^{(2)}t_i^{+(N_\beta\gamma)}, \quad \gamma = 1, \dots, N_\gamma \quad (47)$$

$${}^{(3)}t_i^{+(\beta 1)} = {}^{(3)}t_i^{+(\beta N_\gamma)}, \quad \beta = 1, \dots, N_\beta \quad (48)$$

Using Equations (4) and (5) with Equations (10) and (11) gives

$${}^{(2)}t_i^{\pm(\beta\gamma)} = J_{2i(10)}^{(\beta\gamma)} \pm \frac{h_\beta}{2} J_{2i(00)}^{(\beta\gamma)}, \quad \beta = 1, \dots, N_\beta, \quad \gamma = 1, \dots, N_\gamma \quad (49)$$

$${}^{(3)}t_i^{\pm(\beta\gamma)} = K_{3i(01)}^{(\beta\gamma)} \pm \frac{l_\gamma}{2} K_{3i(00)}^{(\beta\gamma)}, \quad \beta = 1, \dots, N_\beta, \quad \gamma = 1, \dots, N_\gamma \quad (50)$$

Substituting Equations (8), (9), (15), and (16)

$${}^{(2)}t_i^{\pm(\beta\gamma)} = S_{2i(00)}^{(\beta\gamma)} \pm \frac{6}{h_\beta} S_{2i(10)}^{(\beta\gamma)}, \quad \beta = 1, \dots, N_\beta, \quad \gamma = 1, \dots, N_\gamma \quad (51)$$

$${}^{(3)}t_i^{\pm(\beta\gamma)} = S_{3i(00)}^{(\beta\gamma)} \pm \frac{6}{l_\gamma} S_{3i(01)}^{(\beta\gamma)}, \quad \beta = 1, \dots, N_\beta, \quad \gamma = 1, \dots, N_\gamma \quad (52)$$

Thus, the average stress periodicity conditions, Equations (47) and (48), become

$$S_{2i(00)}^{(1\gamma)} - \frac{6}{h_1} S_{2i(10)}^{(1\gamma)} = S_{2i(00)}^{(N_\beta\gamma)} - \frac{6}{h_{N_\beta}} S_{2i(10)}^{(N_\beta\gamma)}, \quad \gamma = 1, \dots, N_\gamma \quad (53)$$

$$S_{3i(00)}^{(\beta 1)} - \frac{6}{l_1} S_{3i(01)}^{(\beta 1)} = S_{3i(00)}^{(\beta N_\gamma)} - \frac{6}{l_{N_\gamma}} S_{3i(01)}^{(\beta N_\gamma)}, \quad \beta = 1, \dots, N_\beta \quad (54)$$

Equations (53) and (54) represent the stress continuity conditions at the boundaries of the RUC necessary to enforce periodicity. Similarly, traction continuity between adjacent subcells is given by:

$$S_{2i(00)}^{(\beta\gamma)} - \frac{6}{h_\beta} S_{2i(10)}^{(\beta\gamma)} = S_{2i(00)}^{(\beta+1\gamma)} - \frac{6}{h_{\beta+1}} S_{2i(10)}^{(\beta+1\gamma)}, \quad \beta = 1, \dots, N_\beta - 1, \quad \gamma = 1, \dots, N_\gamma \quad (55)$$

$$S_{3i(00)}^{(\beta\gamma)} - \frac{6}{l_\gamma} S_{3i(01)}^{(\beta\gamma)} = S_{3i(00)}^{(\beta\gamma+1)} - \frac{6}{l_{\gamma+1}} S_{3i(01)}^{(\beta\gamma+1)}, \quad \beta = 1, \dots, N_\beta, \quad \gamma = 1, \dots, N_\gamma - 1 \quad (56)$$

2.6 Summary of Global Equations

The number of unknown microvariables in the displacement expansion, Equation (18), is $15N_\beta N_\gamma$. The governing equations, Equation (17) provide $3N_\beta N_\gamma$ relations for the unknown microvariables while Equations (43) and (44) provide $3(N_\beta + N_\gamma)$ relations, Equations (45) and (46) provide $3[(N_\beta - 1)N_\gamma + N_\beta(N_\gamma - 1)]$ relations, Equations (53) and (54) provide $3(N_\beta + N_\gamma)$ relations, and Equations (55) and (56) provide $3[(N_\beta - 1)N_\gamma + N_\beta(N_\gamma - 1)]$ relations, which yields a total of $15N_\beta N_\gamma$ linear equations for the unknown microvariables.

This system of equations can be expressed as

$$\mathbf{KU} = \mathbf{f} \quad (57)$$

where \mathbf{K} , the structural stiffness matrix, contains geometric and mechanical constitutive information from each of the subcells in the RUC. The displacement vector \mathbf{U} contains the unknown displacement microvariables for each subcell.

$$\mathbf{U} = [\mathbf{U}^{(11)}, \dots, \mathbf{U}^{(N_\beta N_\gamma)}] \quad (58)$$

and

$$\mathbf{U}^{(\beta\gamma)} = [\mathbf{W}_{(00)}^{(\beta\gamma)}, \mathbf{W}_{(10)}^{(\beta\gamma)}, \mathbf{W}_{(01)}^{(\beta\gamma)}, \mathbf{W}_{(20)}^{(\beta\gamma)}, \mathbf{W}_{(02)}^{(\beta\gamma)}] \quad (59)$$

where the vectors $\mathbf{W}_{(\mathbf{mn})}^{(\beta\gamma)}$ contain the three components of that displacement microvariable for that particular subcell

$$\mathbf{W}_{(\mathbf{mn})}^{(\beta\gamma)} = [W_{1(mn)}^{(\beta\gamma)}, W_{2(mn)}^{(\beta\gamma)}, W_{3(mn)}^{(\beta\gamma)}] \quad (60)$$

The force vector \mathbf{f} contains details of the applied average strains $\bar{\epsilon}_{ij}$. To prevent rigid body motion, the displacement of the corners of the RUC are pinned and those equations are eliminated from Equation (57).

Solving Equation (57) yields a strain concentration matrix that relates the local, average subcell strains to the global, applied, average strains.

$$\boldsymbol{\epsilon}^{(\beta\gamma)} = \mathbf{A}_{\mathbf{HF}}^{(\beta\gamma)} \bar{\boldsymbol{\epsilon}} \quad (61)$$

Once the local strains are obtained, the local stresses are readily determined through the local constitutive laws, Equation (20). The average global stresses are simply the volume average of the local stresses.

$$\bar{\boldsymbol{\sigma}} = \frac{1}{HL} \sum_{\beta=1}^{N_\beta} \sum_{\gamma=1}^{N_\gamma} h_\beta l_\gamma \bar{\boldsymbol{\sigma}}^{(\beta\gamma)} \quad (62)$$

where $\bar{\boldsymbol{\sigma}}^{(\beta\gamma)}$ are the average subcell stresses.

The global, composite constitutive relationship is taken to be

$$\bar{\boldsymbol{\sigma}} = \mathbf{C}^* \bar{\boldsymbol{\epsilon}} \quad (63)$$

Thus, the effective elastic stiffness matrix for the composite is given by substituting Equations (61) and (62) into Equation (63).

$$\mathbf{C}^* = \frac{1}{HL} \sum_{\beta=1}^{N_\beta} \sum_{\gamma=1}^{N_\gamma} h_\beta l_\gamma \mathbf{C}^{(\beta\gamma)} \mathbf{A}_{\mathbf{HF}}^{(\beta\gamma)} \quad (64)$$

It should be noted that HFGMC was reformulated using the displacement continuity conditions to reduce the overall number of unknown microvariables, thus reducing computer memory requirements and computational cost. The reader is referred to [Bansal and Pindera (2004); Aboudi *et al.* (2012)] for details on this reformulation.

3 Modeling Constituent-Level Post-Peak Strain Softening with the Smeared Crack Band Approach

HFGMC is an efficient (relative to fully numerical methods), useful tool for modeling details of the microstructure of a composite material. Additionally, it is readily amenable for implementation into a multiscale framework. Although, physics-based, discretization objective, progressive failure constitutive models must be in place for the constituents of the composite to accurately predict the response of a structure that is a damaging. For pre-peak loading (i.e. positive-definite tangent stiffness tensor), there are a multitude of non-linear elasticity, plasticity, continuum damage mechanics, and viscoelastic/plastic theories available that can predict the evolution of the appropriate mechanisms in the composite. However when the local fields enter

the post-peak regime of the stress-strain laws, most of these theories breakdown in a numerical setting and display pathological mesh dependence [*Bažant and Cedolin (1979); Pietruszczak and Mroz (1981)*].

The lack of positive definiteness of the elastic, or inelastic, tangent stiffness tensor leads to imaginary wave speeds in the material. The longitudinal wave speed in an isotropic material is given by

$$c_L = \sqrt{\frac{E(1 - \nu)}{\rho(1 + \nu)(1 - 2\nu)}} \quad (65)$$

where c_L is the wave velocity, E is the Young's modulus of the material, ν is the Poisson's ratio, and ρ is the material density. A one-dimensional approximation yields $v = \sqrt{\frac{E}{\rho}}$. The existence of an imaginary wave speed results in a boundary value problem that is ill-posed *Bažant and Cedolin (1979); Pietruszczak and Mroz (1981); deBorst (1987); Bažant and Cedolin (1991)*. Physically, a material must possess a positive-definite tangent stiffness tensor, and in fact, at the micro-scale the material tangent stiffness tensor always remains positive-definite. However for practical purposes, engineers must model structures at scales much larger than the flaws in the material, and the homogenized continuum representation of a material with nucleation and propagation of discontinuities, such as cracks or voids, exhibits post-peak strain softening in the macroscopic, homogenized, stress-strain response. This homogenized response is assumed to govern over a suitable volume of the material, appropriate to the microstructure of the material. Loss of positive-definiteness of the tangent stiffness tensor leads to a material instability which manifests as a localization of damage into the smallest length scale in the continuum problem [*Bažant and Cedolin (1991)*]. In GMC or HFGMC this is a single subcell. Thus, the post-peak softening strain energy is dissipated over the volume of the subcell that the damage localizes to. Since a stress-strain relationship prescribes the energy density dissipated during

the failure process, the total amount of energy dissipated in the subcell decreases as the size of the element is reduced, and in the limit zero energy is required to fail the structure.

A simple way to remedy this non-physical behavior in a numerical setting is to judiciously scale the post-peak softening slope of the stress-strain constitutive law. Then, the failure energy density dissipated becomes a function of the characteristic length of discretized continuum. *Bažant* (1982); *Bažant and Oh* (1983) first proposed a crack band model in which post-peak softening damage (herein referred to as failure) in the material was assumed to occur within a band. The post-peak slope of the material constitutive law was scaled by the characteristic length of the finite element exhibiting failure; such that, the total strain energy release rate in the element, upon reaching a state of zero stress, and the material fracture toughness were coincident. In this reference, equivalence between this smeared crack approach and a line crack approach is presented. Subsequently, *Bažant and Cedolin* (1983) exhibited propagation of a crack band not aligned with the mesh bias. In this work, the crack band model is implemented within the HFGMC framework, in the MAC/GMC suite of micromechanics codes developed at the NASA Glenn Research Center [*Bednarczyk and Arnold* (2002a,b)], and used to analyze crack band growth in composite RUCs. The following subsections provide theoretical details on the crack band model.

3.1 Physical Behavior of Crack band

The smeared crack band model is meant to capture the behavior of a region of a material wherein numerous microcracks have initiated and they coalesce to form a larger crack. Figure 6 displays a crack band of width w_c embedded in a continuum. The domain of the crack band is denoted as Ω' and the remaining continuum as Ω . The crack band is oriented within the continuum such that, for a given point within the crack band, the unit vector normal to the crack band is \mathbf{n} .

The total energy dissipated during the failure process is dissipated over Ω' , and the size w_c of Ω' is a material property directly related to the material fracture toughness [Bazant and Oh (1983)].

$$w_c = \frac{2\mathcal{G}_C}{\sigma_C^2} \left(\frac{1}{E} - \frac{1}{E_T} \right)^{-1} \quad (66)$$

where σ_C is the critical stress for initiation of the post-peak regime in the 1D material stress-strain law (given in Figure 7a), and E_T is the negative tangent slope in that regime. The fracture toughness \mathcal{G}_C , or critical strain energy release rate, of the material is given by the area under the 1D traction-separation law (Figure 7b) which governs the cohesive response of the separation of crack faces as a crack propagates in the material. The energy density dissipated during failure W_F is related to the the material fracture toughness by the characteristic length in the material.

$$\mathcal{G}_C = w_c W_F \quad (67)$$

3.2 Numerical Implementation of Crack Band Model in GMC/HFGMC

The crack band model is implemented in the HFGMC micromechanical framework. The local subcell fields are used to govern crack band evolution in the constituents of the composite. Figure 8 shows the discretization of the continuum displayed in Figure 6. A magnified view of the crack band embedded in a single subcell is also displayed in Figure 8. Since the all of the energy dissipated in the crack band is smeared over the subcell volume, the subcell must be large enough to contain the crack band of width w_c . Note that Figure 8 shows a 2D geometry for illustrative purposes, but the crack bands can also evolve in a general 3D space.

3.2.1 Mode I Crack Band Growth Under Tensile Principal Stress

The orientation of the crack band in subcell $\beta\gamma$ is given by the vector $\mathbf{n}_1^{(\beta\gamma)}$ (see Figure 8) and is determined from the local principal stress state $(\bar{\sigma}_1^{(\beta\gamma)}, \bar{\sigma}_2^{(\beta\gamma)}, \bar{\sigma}_3^{(\beta\gamma)})$. In a monolithic material, cracks orient such that the crack tips are always subjected to pure mode I (opening mode) conditions unless there are constraints that limit the crack orientation. In a micromechanical analysis the composite material is composed of separate, monolithic constituents; thus, in the matrix, the crack band runs perpendicular to $\bar{\sigma}_1^{(\beta\gamma)}$, the principal stress with the largest magnitude, $|\bar{\sigma}_1^{(\beta\gamma)}| > |\bar{\sigma}_2^{(\beta\gamma)}| > |\bar{\sigma}_3^{(\beta\gamma)}|$, if $\bar{\sigma}_1^{(\beta\gamma)} \geq 0$ (tensile). Under these conditions, a crack oriented as such, is subjected to pure mode I loading, locally. Although, the resulting global behavior may appear to be mixed mode because of the influence of the fibers on the matrix crack band path. Crack orientation and evolution is determined differently if $\bar{\sigma}_1^{(\beta\gamma)} < 0$ as described in 3.2.2. The characteristic length of the subcell $l_C^{(\beta\gamma)}$ is determined as the dimension of the subcell running parallel to $\mathbf{n}_1^{(\beta\gamma)}$. Crack band initiation is determined using a very simple, but physical, maximum stress criterion.

$$\frac{\bar{\sigma}_1^{(\beta\gamma)}}{\sigma_C^{(\beta\gamma)}} = 1, \quad \bar{\sigma}_1^{(\beta\gamma)} \geq 0 \quad (68)$$

where $\sigma_C^{(\beta\gamma)}$ is the cohesive strength of the crack band. Once the crack band has initiated, the crack band orientation is fixed as time evolves.

Once the crack band orientation has been calculated, the subcell compliance is rotated into the principal frame using the transformation matrix.

$$\mathbf{T} = [\mathbf{n}_1^{(\beta\gamma)} \mathbf{n}_2^{(\beta\gamma)} \mathbf{n}_3^{(\beta\gamma)}][\mathbf{e}_1 \mathbf{e}_2 \mathbf{e}_3] \quad (69)$$

where $\mathbf{n}_1^{(\beta\gamma)}$, $\mathbf{n}_2^{(\beta\gamma)}$, and $\mathbf{n}_3^{(\beta\gamma)}$ are the principal stress directions, and \mathbf{e}_1 , \mathbf{e}_2 , and \mathbf{e}_3 are the unit basis vectors. All material degradation due to crack band evolution is

imposed on the rotated compliance $\bar{\mathbf{S}}^{(\beta\gamma)}$, the components of which are given by:

$$\bar{S}_{ijkl}^{(\beta\gamma)} = T_{pi}T_{qj}S_{pqrs}^{(\beta\gamma)}T_{kr}T_{ls} \quad (70)$$

The strain energy released during the formation of new surfaces corresponding to the growth of cracks within the crack band is assumed to be dissipated over the entire subcell volume. Therefore, the post-peak softening slope $E_{IT}^{(\beta\gamma)}$, and the strain at which a the principal stress state is zero, is calculated using the characteristic length of the subcell $l_C^{(\beta\gamma)}$ and the material fracture toughness $\mathcal{G}_{IC}^{(\beta\gamma)}$ (see Figure 7a).

$$\epsilon_F^{(\beta\gamma)} = \frac{2\mathcal{G}_{IC}^{(\beta\gamma)}}{\sigma_C^{(\beta\gamma)}l_C^{(\beta\gamma)}} \quad (71)$$

$$E_{IT}^{(\beta\gamma)} = \left(\frac{1}{\bar{E}_{110}} - \frac{\epsilon_F^{(\beta\gamma)}}{\sigma_C^{(\beta\gamma)}} \right)^{-1} \quad (72)$$

where \bar{E}_{110} is the undamaged, axial Young's modulus in the principal frame. It should be noted that $E_{IT}^{(\beta\gamma)}$ must be less than zero; therefore, by Equations (71) and (72), a restriction is placed on the maximum allowable subcell size.

$$l_C^{(\beta\gamma)} < \frac{2\mathcal{G}_{IC}^{(\beta\gamma)}\bar{E}_{110}}{\sigma_C^{(\beta\gamma)}} \quad (73)$$

The local, rotated, subcell strain state $\bar{\epsilon}_i^{(\beta\gamma)}$

$$\left\{ \begin{array}{c} \bar{\epsilon}_1^{(\beta\gamma)} \\ \bar{\epsilon}_2^{(\beta\gamma)} \\ \bar{\epsilon}_3^{(\beta\gamma)} \end{array} \right\} = \left\{ \begin{array}{c} T_{1i}^{(\beta\gamma)}\bar{\epsilon}_{ij}^{(\beta\gamma)}T_{1j}^{(\beta\gamma)} \\ T_{2i}^{(\beta\gamma)}\bar{\epsilon}_{ij}^{(\beta\gamma)}T_{2j}^{(\beta\gamma)} \\ T_{3i}^{(\beta\gamma)}\bar{\epsilon}_{ij}^{(\beta\gamma)}T_{3j}^{(\beta\gamma)} \end{array} \right\} \quad (74)$$

is used to degrade the rotated compliance components. The scalar damage factor

$D^{(\beta\gamma)}$ is calculated using the rotated strain corresponding to $\bar{\sigma}_1^{(\beta\gamma)}$.

$$D^{(\beta\gamma)} = 1 + \frac{E_{IT}^{(\beta\gamma)} \left(\epsilon_C^{(\beta\gamma)} - \bar{\epsilon}_1^{(\beta\gamma)} \right)}{\bar{E}_{110} \bar{\epsilon}_1^{(\beta\gamma)}} \quad (75)$$

where $\epsilon_C^{(\beta\gamma)}$ is the value of $\bar{\epsilon}_1^{(\beta\gamma)}$ when the initiation criterion, Equation (68), is satisfied. If $D^{(\beta\gamma)}$ is less than zero, no damage occurs, and a maximum damage level of one corresponds to a zero stress state on the softening stress-strain curve. Also, damage healing is inadmissible.

$$\dot{D}^{(\beta\gamma)} \geq 0 \quad (76)$$

Components of the rotated compliance matrix are degraded with the damage factor.

$$\bar{\mathbf{S}}^{(\beta\gamma)} = \begin{bmatrix} \frac{\bar{S}_{1111}^{(0\beta\gamma)}}{(1 - D^{(\beta\gamma)})} & \bar{S}_{1122}^{(\beta\gamma)} & \bar{S}_{1133}^{(\beta\gamma)} & 0 & 0 & 0 \\ \bar{S}_{1122}^{(\beta\gamma)} & \bar{S}_{2222}^{(\beta\gamma)} & \bar{S}_{2233}^{(\beta\gamma)} & 0 & 0 & 0 \\ \bar{S}_{1133}^{(\beta\gamma)} & \bar{S}_{2233}^{(\beta\gamma)} & \bar{S}_{3333}^{(\beta\gamma)} & 0 & 0 & 0 \\ 0 & 0 & 0 & \bar{S}_{2323}^{(\beta\gamma)} & 0 & 0 \\ 0 & 0 & 0 & 0 & \frac{\bar{S}_{1313}^{(0\beta\gamma)}}{(1 - D^{(\beta\gamma)})} & 0 \\ 0 & 0 & 0 & 0 & 0 & \frac{\bar{S}_{1212}^{(0\beta\gamma)}}{(1 - D^{(\beta\gamma)})} \end{bmatrix} \quad (77)$$

Since the crack band orientation is fixed upon initiation, the $\bar{S}_{1313}^{(\beta\gamma)}$ and $\bar{S}_{1212}^{(\beta\gamma)}$ shear compliances in the rotated frame are degraded, as well as the $\bar{S}_{1111}^{(\beta\gamma)}$ compliance, so that the crack band faces normal to $\mathbf{n}_1^{(\beta\gamma)}$ are free of normal and shear tractions when

all of the crack band energy has been dissipated (i.e. $l_C^{(\beta\gamma)}W_F^{(\beta\gamma)} = \mathcal{G}_{IC}^{(\beta\gamma)}$). Once the compliance in the rotated frame is degraded, the compliance is transformed back to the global frame to yield the new subcell compliance.

$$S_{ijkl}^{(\beta\gamma)} = T_{pi}^{-1}T_{qj}^{-1}\bar{S}_{pqrs}^{(\beta\gamma)}T_{kr}^{-1}T_{ls}^{-1} \quad (78)$$

Note that, damage introduced in the principal frame, through Equation (77), can induce normal-shear coupling in the global frame.

3.2.2 Mode II Crack Band Growth Under Compressive Principal Stress

Crack band growth under pure mode I conditions are energetically favorable; however, conditions arise, under which, mode I crack growth is not possible. For instance, the crack cannot grow under in mode I if the normal traction at the crack tip is compressive. This occurs when the principal stress with the maximum magnitude is compressive ($\bar{\sigma}_1^{(\beta\gamma)} < 0$). However, experimental data shows that monolithic materials subjected to global compression will eventually fracture.

In brittle and quasi-brittle materials, it has been shown that local, internal friction results in shear (mode II) fracture when the monolithic material is subjected to compressive stresses [*Hoek and Bieniawski (1965); Horii and Nemat-Nasser (1986); Ashby and Sammis (1990); Chen and Ravichandran (2000)*]. Consequently, if $\bar{\sigma}_1^{(\beta\gamma)} < 0$ it is assumed that the crack band is aligned with plane of maximum shear stress $\bar{\tau}^{(\beta\gamma)}$ in the matrix subcell and a Mohr-Coulomb failure criterion will be used to indicate crack band initiation under maximum principal compression.

$$\frac{\bar{\tau}_E^{(\beta\gamma)}}{\tau_C^{(\beta\gamma)}} = 1, \quad \bar{\sigma}_1^{(\beta\gamma)} < 0 \quad (79)$$

where $\tau_C^{(\beta\gamma)}$ is the cohesive shear strength of the matrix, and $\bar{\tau}_E^{(\beta\gamma)}$ is an effective shear

stress that includes the influence of the traction normal to the crack band $\bar{\sigma}_n^{(\beta\gamma)}$.

$$\bar{\tau}_E^{(\beta\gamma)} = |\bar{\tau}^{(\beta\gamma)}| + \mu_i \bar{\sigma}_n^{(\beta\gamma)} \quad (80)$$

where μ_i is the internal friction coefficient and must lie between $0 < \mu_i \leq 1.5$ to obtain physically reasonable surface friction coefficient [Chen and Ravichandran (2000)]. Since the principal stress with the largest magnitude is compressive, the traction normal to the maximum shear stress plane $\bar{\sigma}_n^{(\beta\gamma)}$ must also be compressive. Hence, in Equation (80), an increase in the normal compressive stress will yield a reduction in the effective shear stress and an increase in apparent shear strength. Taliercio and Sagramoso (1995) derived relationships between internal friction coefficient, shear strength, the tensile strength and compressive strength of the material, yielding an expression for μ_i in terms of $\sigma_C^{(\beta\gamma)}$ and $\tau_C^{(\beta\gamma)}$.

$$\mu_i = \tan \left\{ \sin^{-1} \left[\frac{\left(2\tau_C^{(\beta\gamma)}\right)^2 - \sigma_C^{(\beta\gamma)^2}}{\left(2\bar{\tau}^{(\beta\gamma)}\right)^2 + \sigma_C^{(\beta\gamma)^2}} \right] \right\} \quad (81)$$

Similar criteria are used for shear failure under compressive loading in homogenized composite materials [Puck and Schürmann (1998, 2002); Pinho et al. (2005)]. In these theories, the orientation of the crack is not aligned with the plane of maximum shear stress because of the influence of the fibers on the crack path, but rather, orientation is an input to the theories obtained from experimental data. Since the influence of the fibers are explicitly accounted for in the present methodology, the crack may remain oriented with the maximum shear stress plane and the local stress in the matrix will drive the crack path.

Subsequent to mode II crack band initiation via Equation (79), the compliance tensor of the subcell is rotated into the maximum shear stress frame using Equations (69) and (70), where $\mathbf{n}_1^{(\beta\gamma)}$ is a unit-vector perpendicular to the plane of maximum

shear stress. Features of the post-peak softening shear stress-shear strain curve, such as the endpoint and post-peak tangent stiffness, can be calculated from the mode II fracture parameters.

$$\gamma_F^{(\beta\gamma)} = \frac{2\mathcal{G}_{IC}^{(\beta\gamma)}}{\tau_C^{(\beta\gamma)}l_C^{(\beta\gamma)}} \quad (82)$$

$$E_{IIT}^{(\beta\gamma)} = \left(\frac{1}{\bar{G}_{120}} - \frac{\gamma_F^{(\beta\gamma)}}{\tau_C^{(\beta\gamma)}} \right)^{-1} \quad (83)$$

where \bar{G}_{120} is the undamaged, axial shear modulus in the maximum shear stress frame. Again the tangent stiffness $E_{IIT}^{(\beta\gamma)}$ must be less than zero; therefore, Equations (82) and (83) place a restriction is on the maximum allowable subcell size.

$$l_C^{(\beta\gamma)} < \frac{2\mathcal{G}_{IC}^{(\beta\gamma)}\bar{G}_{120}}{\tau_C^{(\beta\gamma)}} \quad (84)$$

The shear strain corresponding to the maximum shear stress $\bar{\gamma}^{(\beta\gamma)}$ is obtained by rotating the strain tensor.

$$\bar{\gamma}^{(\beta\gamma)} = T_{1i}^{(\beta\gamma)}\bar{\epsilon}_{ij}^{(\beta\gamma)}T_{2j}^{(\beta\gamma)} \quad (85)$$

An effective shear strain $\bar{\gamma}_E^{(\beta\gamma)}$ can be defined that is work conjugate with the effective shear stress $tEbg$.

$$\bar{\tau}_E^{(\beta\gamma)}d\bar{\gamma}_E^{(\beta\gamma)} = \bar{\tau}^{(\beta\gamma)}d\bar{\gamma}^{(\beta\gamma)} + \bar{\sigma}_n^{(\beta\gamma)}d\bar{\epsilon}_n^{(\beta\gamma)} \quad (86)$$

where $\bar{\tau}^{(\beta\gamma)}$ and $\bar{\sigma}_n^{(\beta\gamma)}$ are the shear and normal tractions acting on the crack faces oriented parallel to the plane of maximum shear stress, and $\bar{\gamma}^{(\beta\gamma)}$ and $\bar{\epsilon}_n^{(\beta\gamma)}$ are the apparent shear and normal strains with respect to the maximum shear orientation in the subcell, including the effects of crack tip opening displacement. Taking the derivative of Equation (86) with respect to $\bar{\tau}^{(\beta\gamma)}$ yields

$$\frac{\partial\bar{\tau}_E^{(\beta\gamma)}}{\partial\bar{\tau}^{(\beta\gamma)}}d\bar{\gamma}_E^{(\beta\gamma)} = d\bar{\gamma}^{(\beta\gamma)} \quad (87)$$

and along with the derivative of Equation (80) with respect to $\bar{\tau}^{(\beta\gamma)}$

$$\frac{\partial \bar{\tau}_E^{(\beta\gamma)}}{\partial \bar{\tau}^{(\beta\gamma)}} = 1 \quad (88)$$

finally, after integrating, gives:

$$\bar{\gamma}_E^{(\beta\gamma)} = \bar{\gamma}^{(\beta\gamma)} \quad (89)$$

which states that the shear strain in the rotated, maximum shear stress frame and the effective shear strain that is work conjugate to the effective, Mohr-Coulomb shear stress are equivalent.

Thus, $\bar{\gamma}^{(\beta\gamma)}$ is used to degrade the rotated compliance components. The damage factor $D^{(\beta\gamma)}$ is calculated using $\bar{\gamma}$.

$$D^{(\beta\gamma)} = 1 + \frac{E_{III}^{(\beta\gamma)} \left(\gamma_C^{(\beta\gamma)} - \bar{\gamma}^{(\beta\gamma)} \right)}{\bar{G}_{120} \bar{\gamma}^{(\beta\gamma)}} \quad (90)$$

where $\gamma_C^{(\beta\gamma)}$ is the value of $\bar{\gamma}^{(\beta\gamma)}$ when the initiation criterion, Equation (79), is satisfied. In the case of mode II fracture, only the shear moduli are degraded. The normal

direction is subjected to compression, and thus, retains its stiffness.

$$\bar{\mathbf{S}}^{(\beta\gamma)} = \begin{bmatrix} \bar{S}_{1111}^{(\beta\gamma)} & \bar{S}_{1122}^{(\beta\gamma)} & \bar{S}_{1133}^{(\beta\gamma)} & 0 & 0 & 0 \\ \bar{S}_{1122}^{(\beta\gamma)} & \bar{S}_{2222}^{(\beta\gamma)} & \bar{S}_{2233}^{(\beta\gamma)} & 0 & 0 & 0 \\ \bar{S}_{1133}^{(\beta\gamma)} & \bar{S}_{2233}^{(\beta\gamma)} & \bar{S}_{3333}^{(\beta\gamma)} & 0 & 0 & 0 \\ 0 & 0 & 0 & \bar{S}_{2323}^{(\beta\gamma)} & 0 & 0 \\ 0 & 0 & 0 & 0 & \frac{\bar{S}_{1313}^{(\beta\gamma)}}{(1 - D^{(\beta\gamma)})} & 0 \\ 0 & 0 & 0 & 0 & 0 & \frac{\bar{S}_{1212}^{(\beta\gamma)}}{(1 - D^{(\beta\gamma)})} \end{bmatrix} \quad (91)$$

Then, the compliance tensor is rotated back to the global frame using Equation (78).

4 Subcell Mesh Objectivity

The key advantage of using the smeared crack band approach is that it has been verified to provide mesh objective results within an FEM setting; this can also be said for implementation of this model within HFGMC. To illustrate this, a uniform, uniaxial, tensile displacement u was applied to monolithic, doubly-periodic, unit square RUCs in the x_3 -direction. As shown in Figure 9, the levels of subcell refinement ranged from: 35 subcells x 35 subcells, 45 subcells x 45 subcells, 55 subcells x 55 subcells, to 65 subcells x 65 subcells. The elastic properties were chosen to match data for in-situ MY750/HY917/DY063 epoxy matrix [Hinton *et al.* (2004)]. The fracture properties were chosen such that the problem would demonstrate significant post-peak energy dissipation. All properties are given in Table 1. A single subcell, colored red in Figure

9, was given a 10% lower initiation strain than the rest of the domain. Additionally, only the subcells that lie along a horizontal line running through the weaker subcell were allowed to fail because as the damaged region grows, the opposite ends of the damaged region would interact with each other (due to periodicity), as a result of the periodic boundary conditions, altering the damage path and resulting in damage growth that is not self-similar. Restricting the damage path ensures that only subcell dimensions would influence the results from case to case.

The resulting load P in the x_3 -direction is plotted in Figure 10 against the applied displacement for the four different levels of subcell refinement. It is clear that the total strain energy release rate dissipated in the system, and the ultimate load, is insensitive to the dimension of the subcell size. Of course, in more complicated RUCs, a certain level of subcell refinement is necessary to capture the local fields accurately; however, that behavior is not pathological subcell mesh dependence because the solution is bounded.

5 Details of Numerical Models

The smeared crack band model, presented in Section 3.2, is implemented within HFGMC, and it is used to investigate the progression of post-peak softening damage within a unidirectional fiber-reinforced composite RUC. The main objective was to capture the failure evolution of a composite RUC under transverse tension and compression. In tension, the lamina is susceptible to transverse cracking, as evidenced by the scanning electron microscope (SEM) image of a unidirectional composite failed under tension in Figure 11. The behavior of this mechanism is observed to be quite brittle, as is evidenced by tension tests on 90° coupon laminates. However, in compression a network of shear bands develop, accompanied by some matrix cracking and fiber-matrix debonding (see the SEM image in Figure 12) and the stress-strain

response if much more ductile. To emulate these failure modes, a doubly-periodic HFGMC RUC of the 2-3 plane of the composite was created (see Figure 13). This RUC was subjected to global tensile and compressive, transverse, uniaxial strains: $\pm\bar{\epsilon}_{22}$. The constitutive behavior of the matrix subcells follows linear elasticity, coupled with the crack band model for post-peak strain softening formulated earlier. This model is verified against experimental data in Section 6.

A representation of the 2-3 plane of a typical composite lamina (where the 1-axis runs in the longitudinal direction of the fibers and the 2- and 3-axes span the plane of transverse isotropy) was produced to examine the evolution of transverse cracks within the composite. The blueprint for the discrete model is created by randomly placing thirteen circular fibers with a diameter of $5\ \mu\text{m}$ in a square box. The domain was then discretized into a number of subcells. The considered formulation of HFGMC only admits rectangular subcells in doubly-periodic models (parallelepiped in triply-periodic models); so, some of the fiber domains would overlap or lie directly adjacent to one another. An isoparametric formulation of HFGMC has been recently developed by *Haj-Ali and Aboudi* (2010). Mesh objective, subcell interfacial debonding has been formulated for GMC (see *Pineda et al.* (2010a,b)) but has not been fully developed within the HFGMC framework. As a result, thin matrix channels were inserted between any adjacent fibers to avoid arrest of the crack band for non-physical reasons such as the inability of two adjacent fiber to separate. The final architecture and discretization is shown in Figure 13, which contains 81 subcells x 85 subcells. The blue subcells indicate fiber material and the green represent the matrix. The dimensions of the RUC ($21.25\ \mu\text{m} \times 21.25\ \mu\text{m}$) were chosen such that the final fiber volume fraction in Figure 13 would be preserved at 58%, corresponding to the experimental data provided in *Hinton et al.* (2004).

The elastic properties for a Silenka E-glass/MY750/HY917/DY063 lamina were taken from data from the world wide failure exercise WWFE [*Hinton et al.* (2004)].

Elastic properties for Silenka E-glass fiber and MY750/HY917/DY063 epoxy matrix used are given in Table 2. Note that the matrix properties were correlated to represent the in-situ properties of the matrix, which differ significantly from those of the neat material [Ng *et al.* (2010)], and match the global properties of the composite. As a result of this calibration, the isotropic relationship between the shear modulus and the Young’s modulus and Poisson’s ratio of the matrix is not maintained. The fracture properties (also Table 2) were calibrated to produce an ultimate transverse tensile stress of 40 MPa, and the compressive properties were calibrated to match transverse compression data, reported in Hinton *et al.* (2004).

6 Results

6.1 Transverse Tension

A comparison between the tensile results obtained from the HFGMC model and the experiment is provided in Figure 14. Only one data point is given in Hinton *et al.* (2004), implying that the tensile response is linear until ultimate failure. The first peak in the $\bar{\sigma}_{22}$ - $\bar{\epsilon}_{22}$ obtained from HFGMC at $\bar{\sigma}_{22} = 39.76$ MPa and $\bar{\epsilon}_{22} = 0.00244$ was calibrated to match the experimental data, and thus, correlates well. This is expected since the failure parameters were calibrated to match the experimental data. Subsequent to the first peak, the model exhibits a sudden drop in the global stress; however, the RUC then continues to reload in a nonlinear manner. A second peak is achieved at an applied transverse strain of 0.00308 and a transverse stress of 37.97 MPa, which is slightly less than the stress at the first peak. After the second peak, the load carrying capability of the RUC is severely diminished.

The evolution of the tensile crack band in the RUC is presented in Figure 15. At $\bar{\sigma}_{22} = 37.84$ MPa a crack band initiates near the top of the RUC between two fibers (please refer back to Figure 13 for the fiber-matrix architecture). At the ultimate

stress 39.76 MPa, the initial crack band has grown significantly into a fully developed crack band that propagated across the periodic boundary into the bottom of the RUC. The tips of the initial crack band are arrested in lower stress, matrix rich regions. At $\bar{\sigma}_{22} = 35.09$ MPa, after the ultimate stress has been achieved and the RUC is reloading, A new crack band initiates between two adjacent fibers. When the second peak is reached, the subcells composing the second crack band have degraded significantly, and the original crack band has extended further. As the stress drops, Figure 15e, a third crack band initiates. The newest crack band develops rapidly, and the second crack band becomes stagnant. When the RUC has completely failed and can no longer sustain any load, the first and third crack band have bridged to form a nearly continuous crack that has maneuvered around the fiber inclusions and spans the entire height of the RUC. This failure path closely resembles the SEM image of a transverse crack in the glass/epoxy composite shown in Figure 11b, and although the model does not account for fiber-matrix debonding, the model exhibits appreciable matrix failure in matrix subcells adjacent to fiber subcells.

6.2 Transverse Compression

The same HFGMC RUC is loaded in transverse compression and the stress-strain response is compared to the experimental data in Figure 16. The nonlinear behavior of the model and experiment correlate well until the model exhibits catastrophic failure at -104.8 MPa, which is well below the reported ultimate compressive strength of 145 MPa.

Investigations into the failure progression within the RUC reveal the cause of the premature ultimate failure. Figure 17 shows the progression of mode II failure (D_C), resulting from maximum, compressive principal stresses (left column), mode I failure (D_T), resulting from maximum, tensile principal stress (middle column), and the superposition of mode I and mode II failure ($D_T + D_C$, right column) as the

RUC is loaded in global, transverse compression. The first failure initiation occurs between two fibers near the top of the RUC under mode II conditions at a global stress of -65.68 MPa. As the applied strain increases, many mode II crack bands form in angular matrix regions between closely packed fibers. This is exhibited in Figures 17b and 17c. When the global stress reaches -92.88 MPa, a mode I crack band initiates in the top-right corner of the RUC. At the ultimate stress, Figure 17f both the mode I and mode II crack band have evolved. In Figure 17g, shortly after the ultimate stress was reached, a network of angular mode II crack bands has formed. These mode II crack bands are bridged by a horizontal, mode I crack band forming one continuous crack band that has progressed throughout the RUC. When the global stress has dropped severely, in Figure 17h, there is substantial matrix degradation resulting from mode II crack band propagation. Furthermore, one fiber is completely surrounded by crack bands. Comparing Figure 17h to an SEM image of a compressively failed carbon fiber/epoxy laminate in Figure 12b, displays closely resembling failure patterns, indicating that the qualitative failure mode was captured accurately, despite the quantitative discrepancy.

The development of mode I crack bands corresponded to a drop in global stress shortly thereafter. Thus, to determine if the mode I crack bands were responsible for the premature failure of the RUC, the simulation was re-executed but mode I crack band growth was prohibited. The global $\bar{\sigma}_{22}$ - $\bar{\epsilon}_{22}$ response is presented in Figure 16, along with the previous results and experimental data. It can be observed that ultimate failure is delayed considerably until the $\bar{\sigma}_{22} = -146.4$ MPa, which corresponds well to the strength reported in Ref. [Hinton *et al.* (2004)] although the ultimate failure strain 16% higher. Moreover, the majority of the stress-strain response of the RUC matches the experimental data. This indicates that, in the model, the mode II crack bands are responsible for the observed nonlinearity; whereas, the mode I crack bands are responsible for the early onset of ultimate failure, as the mode I fracture

toughness is an order of magnitude lower than mode II.

Extending this observation to the behavior of actual composite would suggest that its non-linearity is controlled by shear band evolution, and the ultimate failure is due to progression of tensile cracks and fiber-matrix debonding. It may be that the size of the RUC (i.e. number of fibers included in the RUC) was too small to get an accurate representation of the quantitative response of the composite under compression, and the growth of the tensile crack band made an unrealistically large impact on the response of the RUC. Further studies evaluating the influence of fiber-matrix architecture on the compressive response of composites needs to be performed. Additionally, adjacent constraining plies with different local architectures, present in the experiment, may have helped to diminish the effect of formation of tensile cracks, which is an effect not captured in this analysis.

The mode II crack band progression, produced by the simulation in which mode I crack band growth was disabled, is displayed in Figure 18. Prior to the initiation of the mode I crack band in Figure 17, Figures 17 and 18 are identical. However as the stress continues beyond the ultimate stress observed in the original simulation, more angular, distributed, mode II crack bands arise, as shown in Figure 18i at the ultimate stress of the simulation with mode I crack band preclusion. Upon ultimate failure, the expansive array of mode II crack bands is almost entirely adjoined and nearly all of the matrix subcells in the RUC have failed. The SEM image, Figure 12b, does not display such extensive failure. This further supports that the failure mode predicted with both mode I and mode II crack bands is more physically correct, and other factors are influencing the discrepancy between the response of the model and the experiment.

7 Conclusions

A mesh objective, smeared crack band model was implemented at the matrix subcell level within the HFGMC micromechanics framework. Mode I crack bands were allowed to propagate normal to the maximum principal stress when the principal stress component with the maximum magnitude was tensile, and the associated strain exceeded a critical value. If the principal stress component with the maximum magnitude was compressive, however, it was assumed that mode I cracks within the crack band could not evolve, and instead, they grew in mode II as a result of Mohr-Coulomb friction, upon satisfaction of a Mohr-Coulomb failure criterion. The mode II crack bands were aligned with the plane of maximum shear stress. Although, the damage model and framework are verified using a polymer matrix composite as an example, the model is applicable to any brittle or quasi-brittle material including ceramics or concrete.

An RUC containing 13, randomly distributed glass fibers in epoxy matrix was simulated under global transverse tension and compression. The results for both cases were compared to experimental data. The tensile response correlated extremely well with the test results. Although, the failure parameters were calibrated to match the experimental data, the successful correlation verifies that the smeared crack band model, utilized within HFGMC, can capture the evolution of brittle transverse cracks. Furthermore, the predicted failure mode mirrored SEM images of composites failed in tension. Under compression, the micromechanics model predicted failure well below the reported compressive strength. This was attributed to the formation of tensile, mode I crack bands in the matrix which exhibit very low fracture toughness. A simulation wherein mode I crack band evolution was restricted, provided quantitative results that more closely agreed with the experiment. However, the failure mode exhibited by the simulation allowing for both mode I and mode II crack bands more closely resembled an SEM image of a compressively failed composite compared to

the latter simulation. This indicates that a sensitivity study on the size and level of refinement of the RUC should be enacted. Future studies will determine the number of fibers in the RUC required to achieve convergence of the stiffness and the failure progression.

Additionally, the response of the RUC to applied intralaminar shear strain $\bar{\gamma}_{12}$ was not enacted. When subjected to in-plane shear loading numerous microcracks form between fibers along the fiber direction in the composite laminae [Ng *et al.* (2010)]. This 3-D effect results in the composite exhibiting a very ductile response in shear. To capture these 3-D, geometric effects with the proposed model, a very complex, 3-D RUC is required.

The RUC examples that were provided are far too computationally expensive for a multiscale analysis. However, insight gained from the micromechanics analysis can be utilized to formulate traction-separation laws, or to postulate fracture toughnesses that include the geometric effects and can be implemented into simpler, more computationally feasible RUCs. To preserve the stress-strain response a consistent strain energy density must exist across the scales. However, the mesh objectivity gained by utilizing the smeared crack band model at the microscale is lost if the SERR is not also preserved across the scales. To accomplish this, a consistent length must be used at both scales. Thus, the volume of the microscale RUC and the volume associated with the corresponding macroscale integration point must be equivalent.

Property	Value
E (GPa)	3.7
ν	0.35
ϵ_C	0.0135
ϵ_C (weak)	0.01215
\mathcal{G}_C (N/mm)	750

Table 1: Elastic and fracture properties used in mesh objectivity study.

Property	Value
E_f (GPa)	74.000
ν_f	0.200
E_m (GPa)	4.65
ν_m	0.350
\mathcal{G}_m	1.4
$\epsilon_C^{(\beta\gamma)}$	0.0167
$\gamma_C^{(\beta\gamma)}$	0.0256
$\mathcal{G}_{IC}^{(\beta\gamma)}$ (N/mm)	0.00076
$\mathcal{G}_{IC}^{(\beta\gamma)}$ (N/mm)	0.00435

Table 2: Elastic and fracture properties used in RUC simulation of 2-3 plane of a Silenka E-Glass/MY750/HY917/DY063 composite lamina.

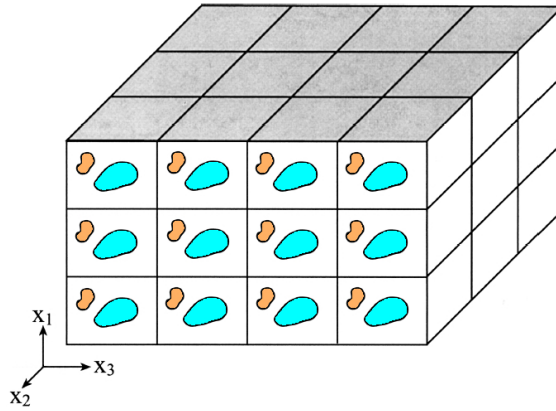


Figure 1: Representation of triply-periodic microstructure of a composite material *Bednarczyk et al. (2010)*.

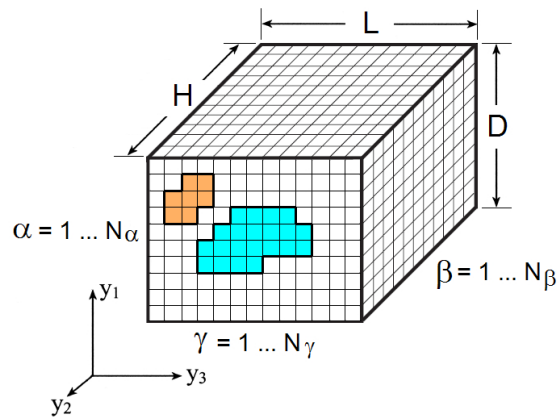


Figure 2: Discretization of a 3D, triply-periodic RUC *Bednarczyk et al. (2010)*.

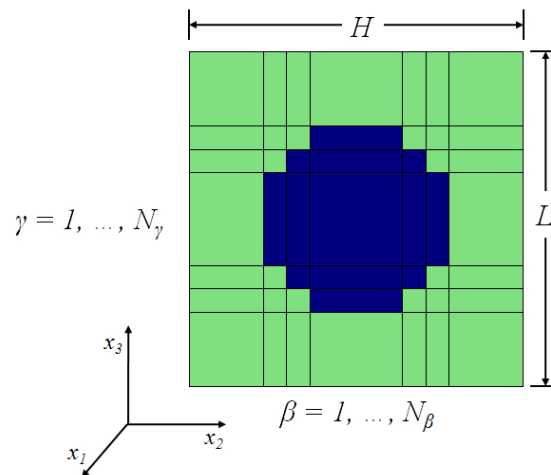


Figure 3: Discretization of a 2D, doubly-periodic RUC.

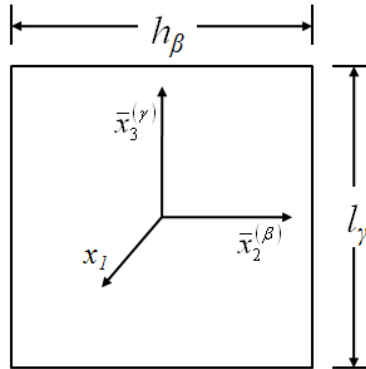


Figure 4: 2D GMC/HFGMC subcell with local coordinate frame.

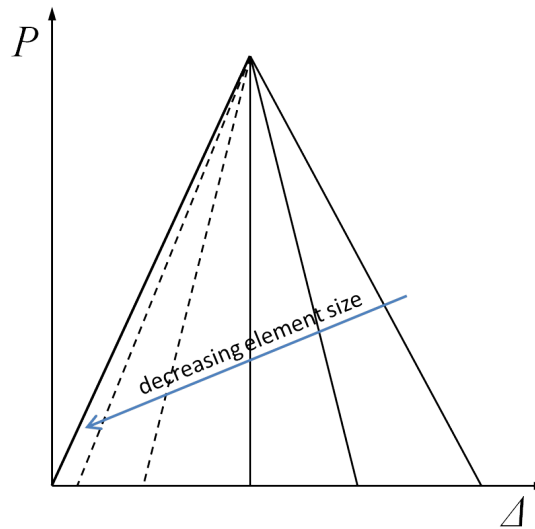


Figure 5: Effects of mesh refinement on overall load-displacement response for a material exhibiting post-peak softening. Dashed lines indicate non-physical snapback.

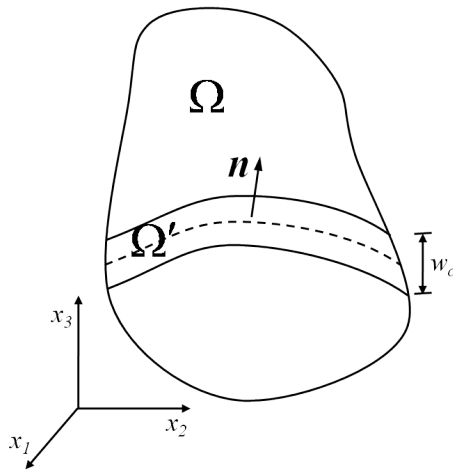


Figure 6: Crack band domain Ω' of width w_c oriented normal to vector \mathbf{n} within a continuum Ω .

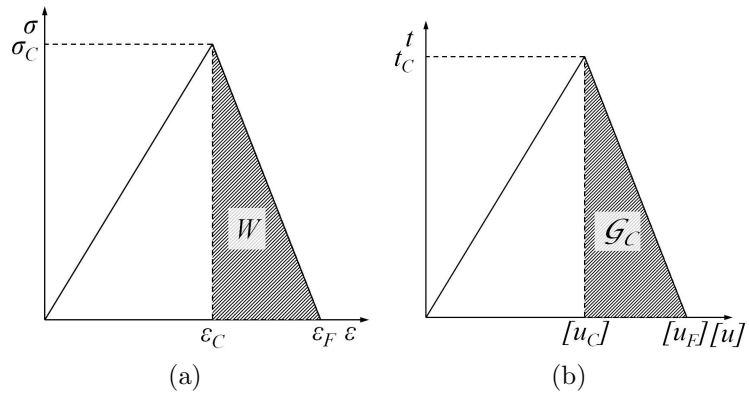


Figure 7: Stress-strain (a) and traction-separation (b) laws governing material behavior. Failure energy density W_F is related to fracture toughness \mathcal{G}_C through the characteristic length.

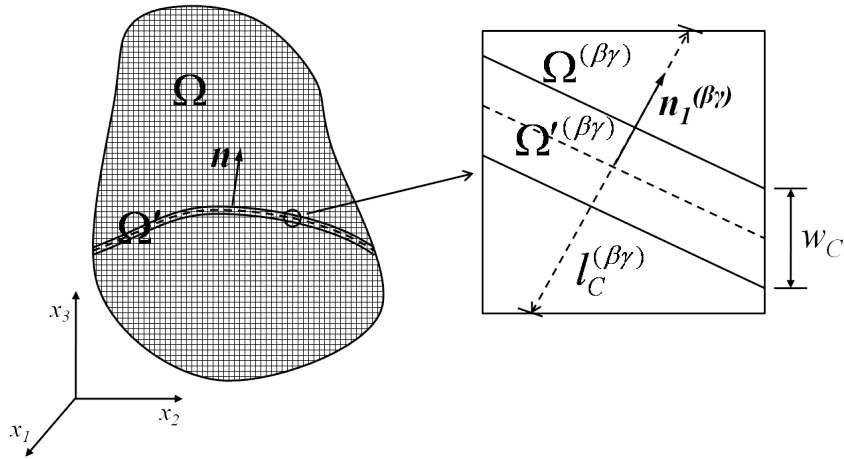


Figure 8: Crack band embedded in discretized continuum. Magnified subcell displays crack band orientation within subcell as well as characteristic length of subcell.

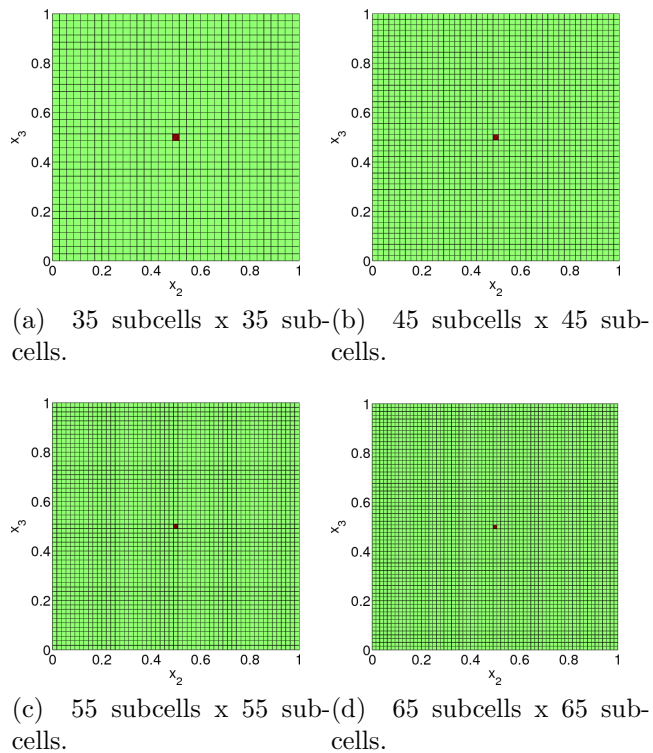


Figure 9: Four subcell meshes used in mesh objectivity study. Red subcell was given a lower crack band initiation strain than others.

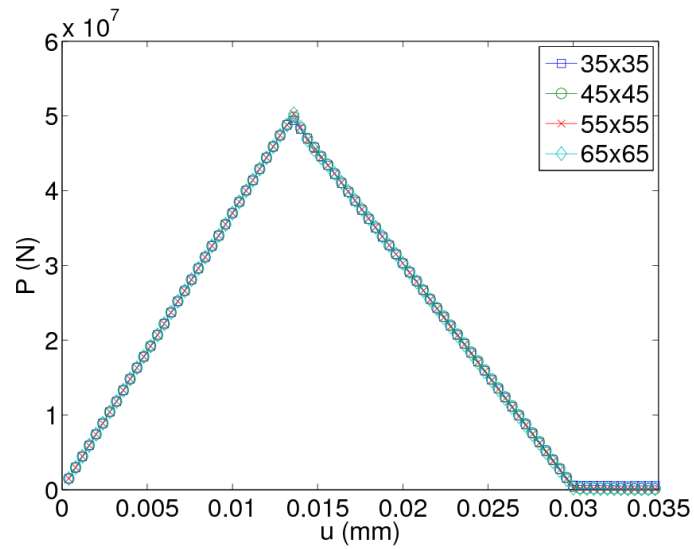
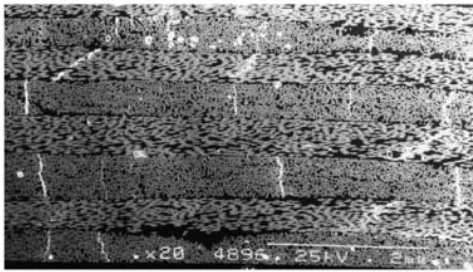
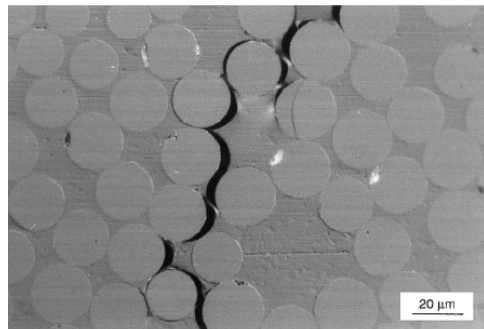


Figure 10: Load versus displacement for four different subcell meshes. Total strain energy release rate and ultimate load are unaffected by mesh refinement.

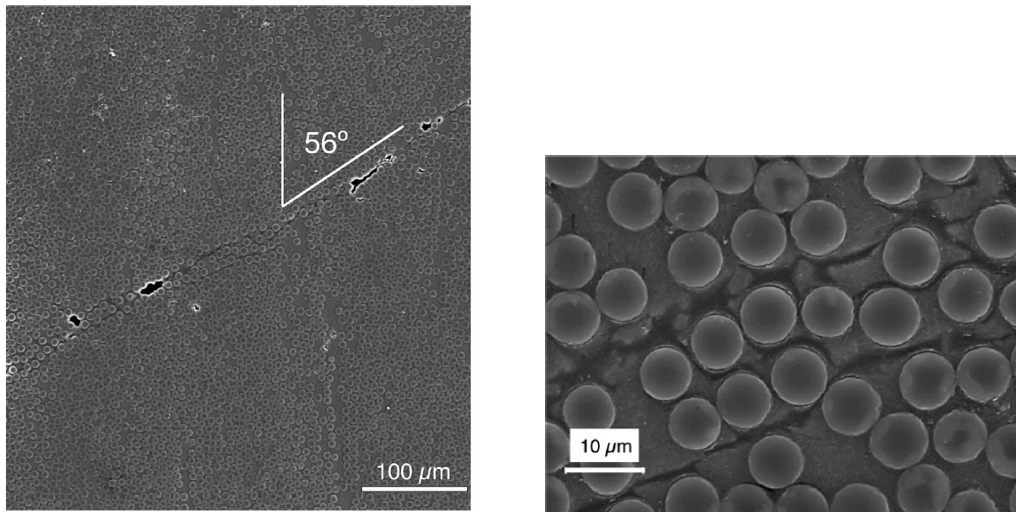


(a) Multiple transverse cracks. [Roberts (2000)].



(b) Magnification of a single transverse crack. [Gamstedt and Sjögren (1999)].

Figure 11: Transverse cracks in glass/epoxy laminates.



(a) Macroscopic failure [Aragonés (2007)].

(b) Localized shear bands and cracks [González and Llorca (2007)].

Figure 12: Transverse compressive failure of carbon fiber/epoxy laminates. Macroscopic failure path observed at an angle. Magnification illustrates shear banding, cracking and fiber-matrix debonding.

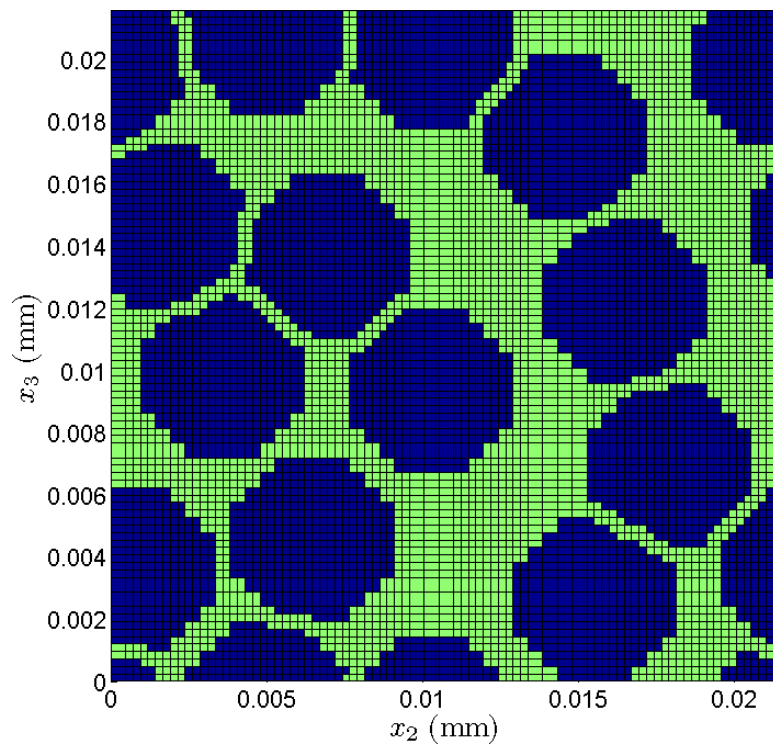


Figure 13: HFGMC mesh used in simulations of RUC in 2-3 plane of lamina containing 13 fibers and a fiber volume fraction of 58%. Subcells/elements occupied by fibers are colored blue, and subcells/elements occupied by matrix are colored green.

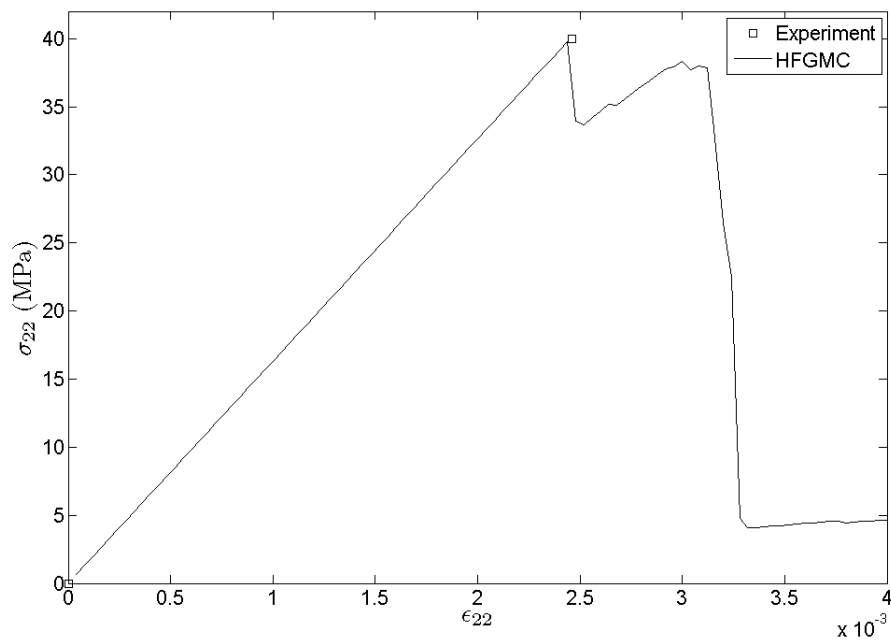
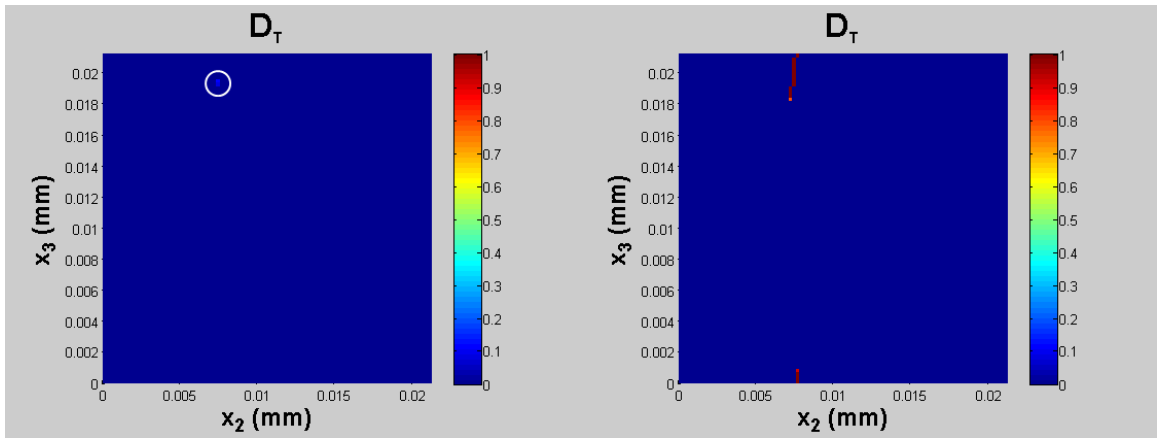
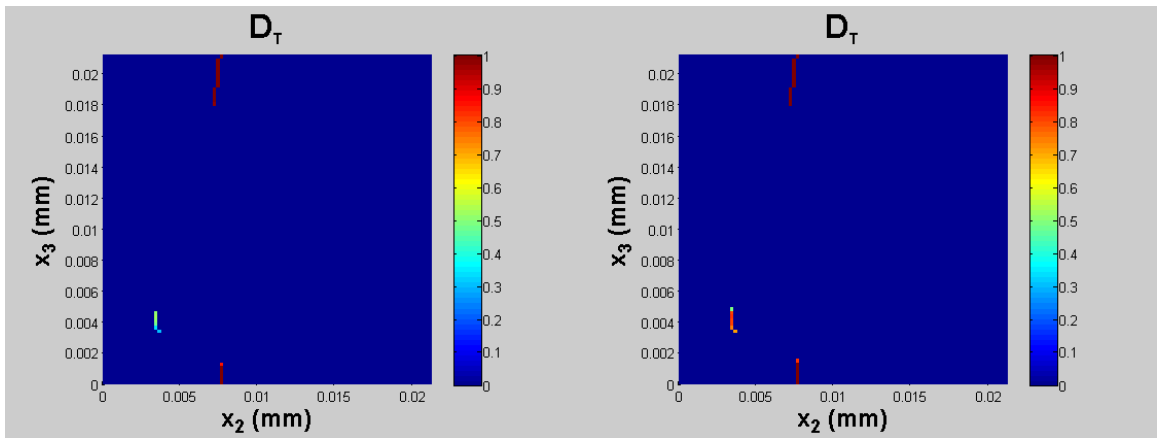


Figure 14: Transverse tensile stress versus transverse strain of E-glass/Epoxy composite from experiment compared to HFGMC micromechanics model.



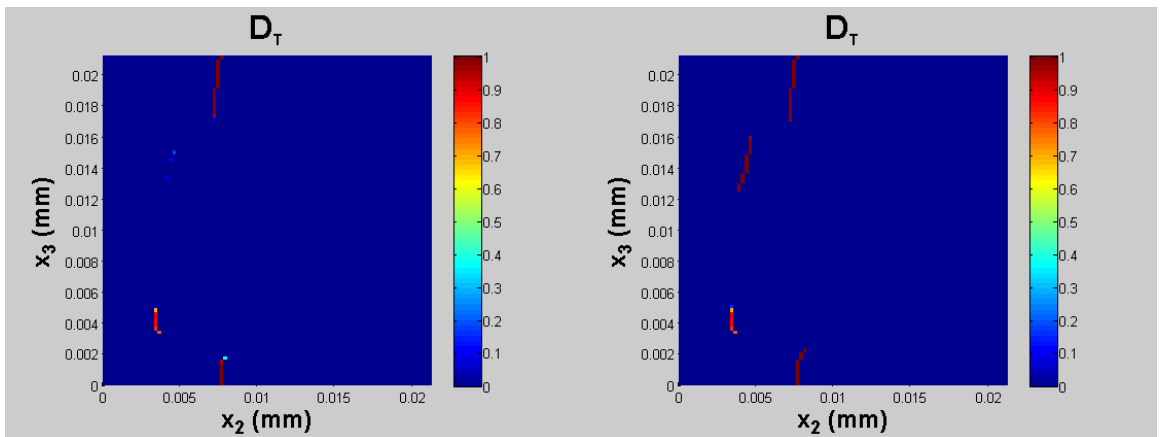
(a) $\epsilon_{22} = 0.00232$, $\sigma_{22} = 37.84$ MPa.

(b) $\epsilon_{22} = 0.00248$, $\sigma_{22} = 39.76$ MPa (First peak stress).



(c) $\epsilon_{22} = 0.00268$, $\sigma_{22} = 35.09$ MPa.

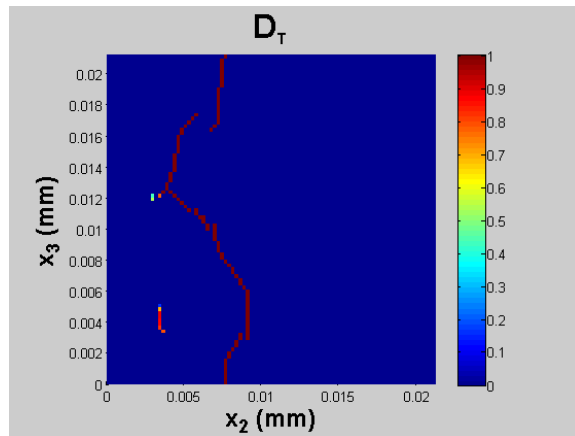
(d) $\epsilon_{22} = 0.00300$, $\sigma_{22} = 38.35$ MPa (Second peak stress).



(e) $\epsilon_{22} = 0.00308$, $\sigma_{22} = 37.88$ MPa.

(f) $\epsilon_{22} = 0.00316$, $\sigma_{22} = 32.68$ MPa.

Figure 15: Evolution of mode I crack band in RUC subjected to applied transverse tensile strain.



(g) $\epsilon_{22} = 0.00336$, $\sigma_{22} = 4.11$ MPa.

Figure 15: Evolution of mode I crack band in RUC subjected to applied transverse tensile strain.

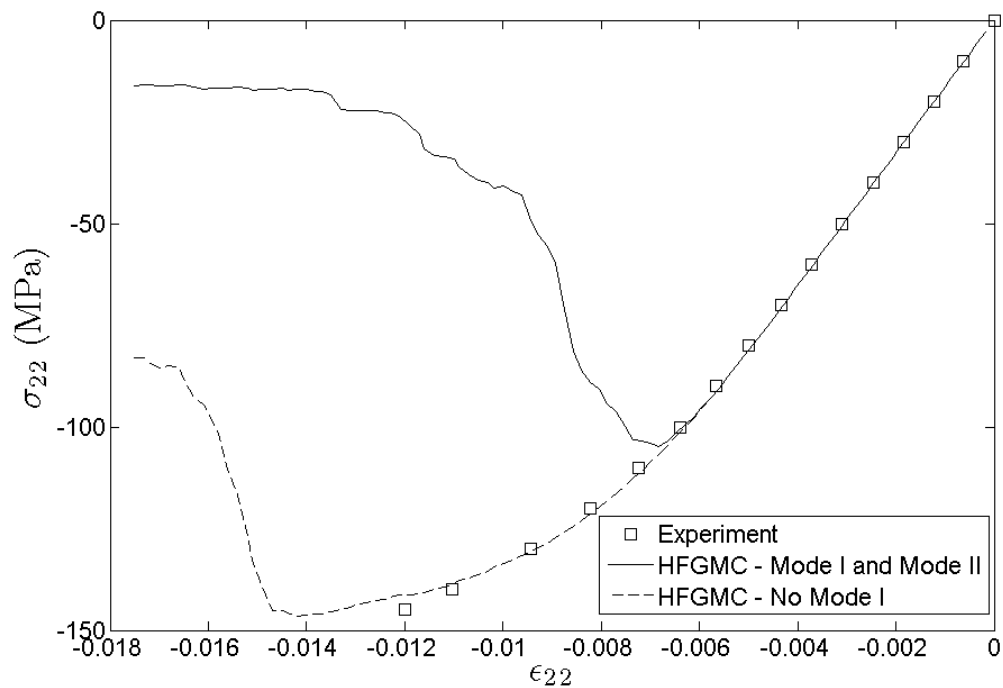
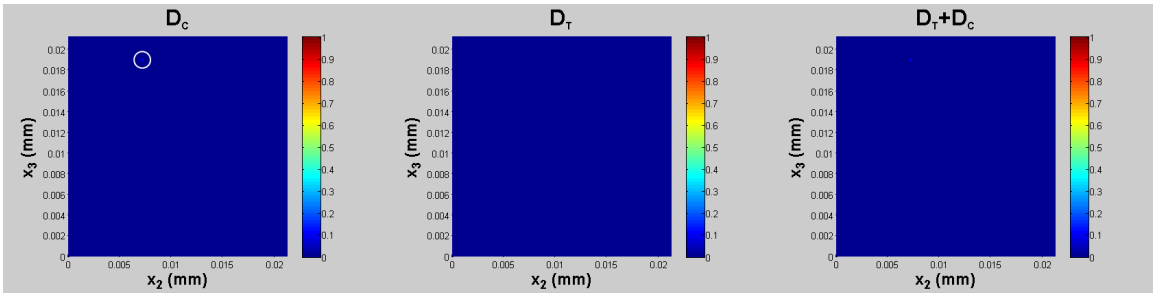
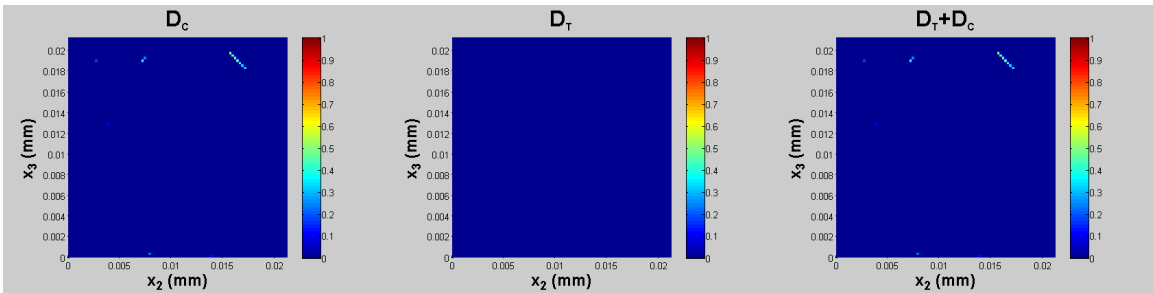


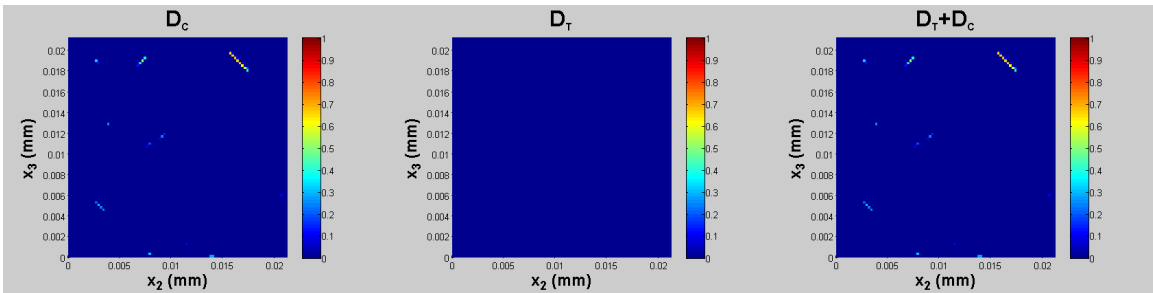
Figure 16: Compressive Transverse stress versus transverse strain of E-glass/Epoxy composite from experiment compared to HFGMC micromechanics model.



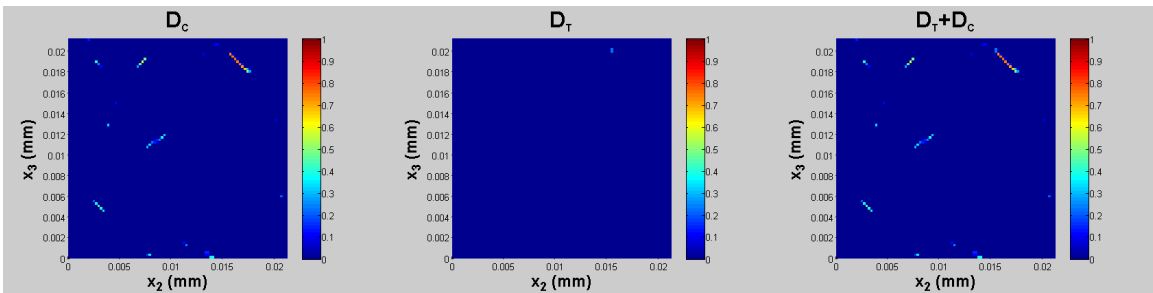
(a) $\epsilon_{22} = -0.00403$, $\sigma_{22} = -65.68$ MPa.



(b) $\epsilon_{22} = -0.00490$, $\sigma_{22} = -79.66$ MPa.

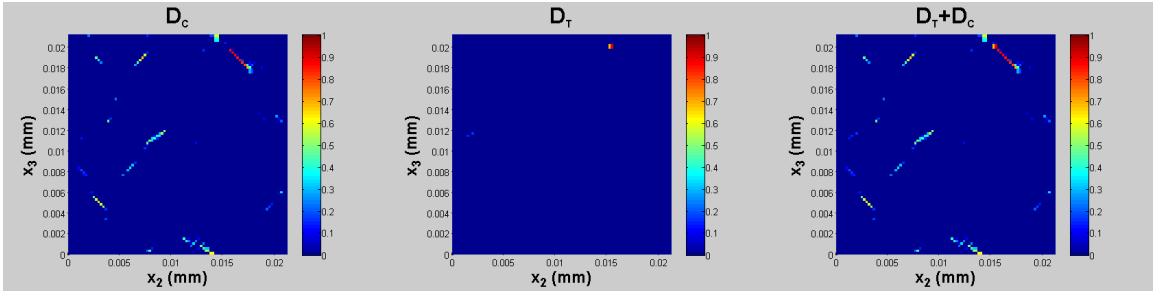


(c) $\epsilon_{22} = -0.00543$, $\sigma_{22} = -87.71$ MPa.

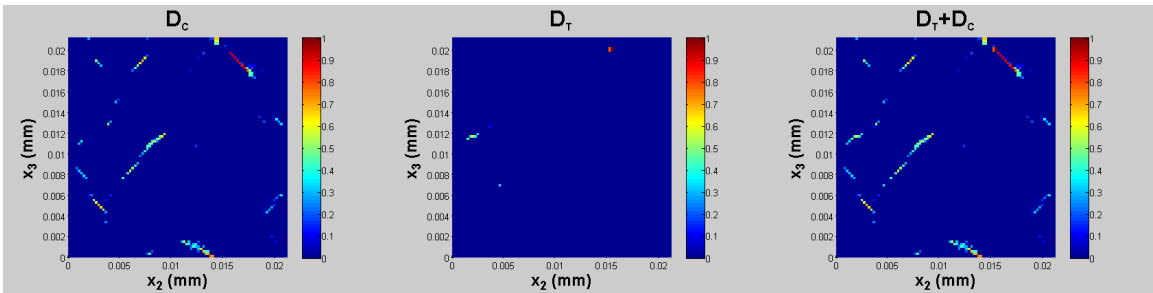


(d) $\epsilon_{22} = -0.00578$, $\sigma_{22} = -92.88$ MPa.

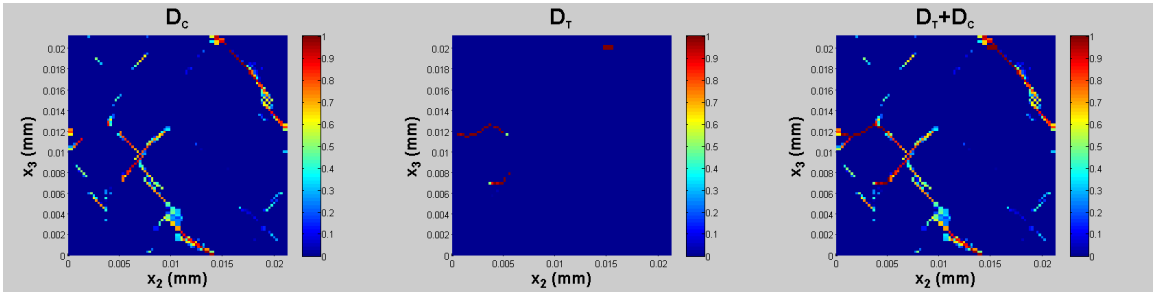
Figure 17: Evolution of mode I (left), mode II (middle), and superposition of mode I and mode II (right) crack band in RUC subjected to applied transverse compressive strain.



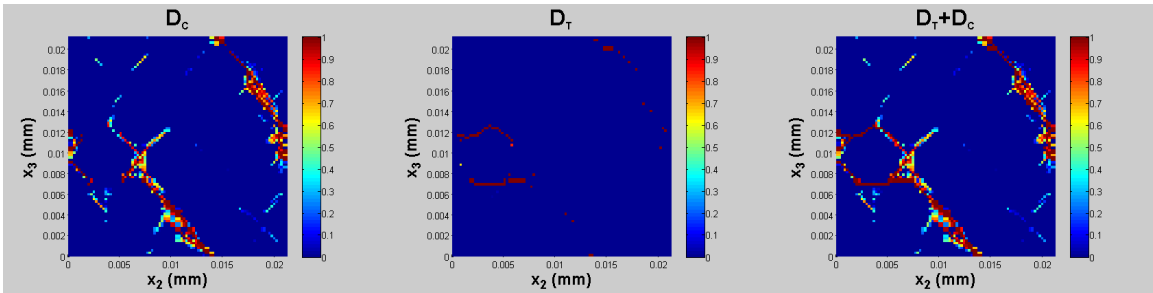
(e) $\epsilon_{22} = -0.00630$, $\sigma_{22} = -99.56$ MPa.



(f) $\epsilon_{22} = -0.00683$, $\sigma_{22} = -104.78$ MPa (ultimate stress).

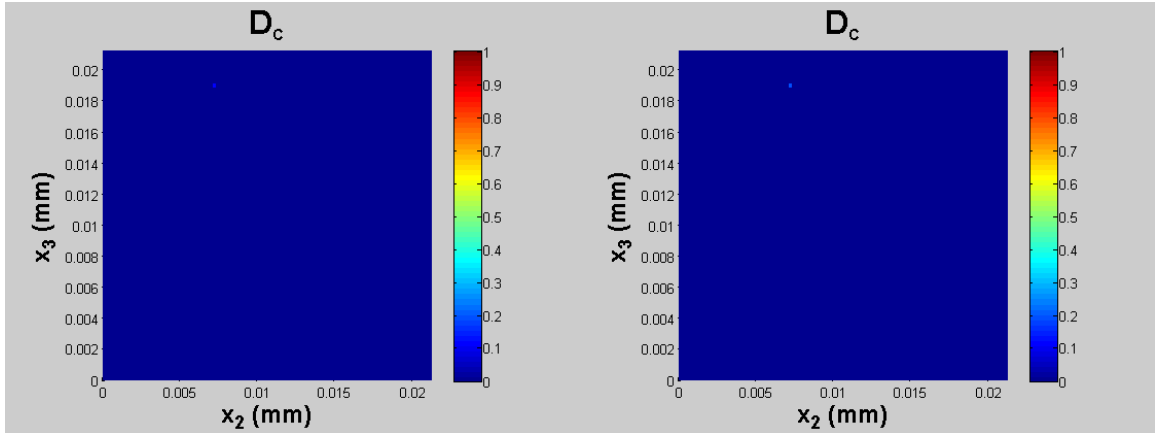


(g) $\epsilon_{22} = -0.00770$, $\sigma_{22} = -96.37$ MPa.



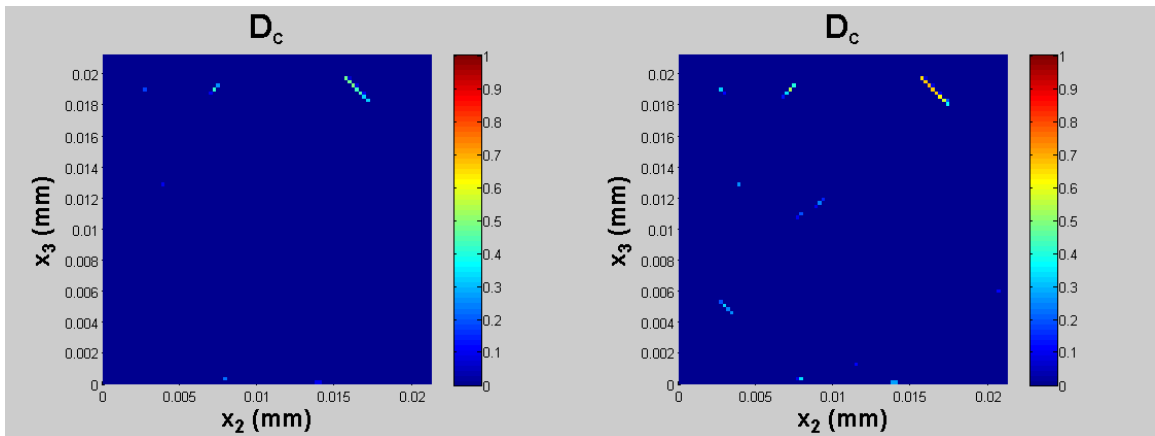
(h) $\epsilon_{22} = -0.01750$, $\sigma_{22} = -16.06$ MPa.

Figure 17: Evolution of mode I (left), mode II (middle), and superposition of mode I and mode II (right) crack band in RUC subjected to applied transverse compressive strain.



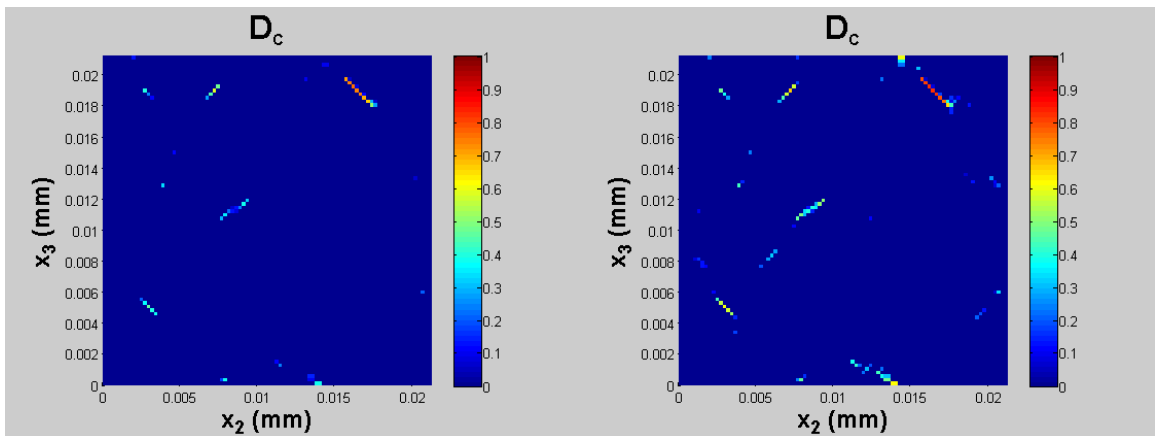
(a) $\epsilon_{22} = -0.00403$, $\sigma_{22} = -65.68$ MPa.

(b) $\epsilon_{22} = -0.00420$, $\sigma_{22} = -68.53$ MPa.



(c) $\epsilon_{22} = -0.00490$, $\sigma_{22} = -79.66$ MPa.

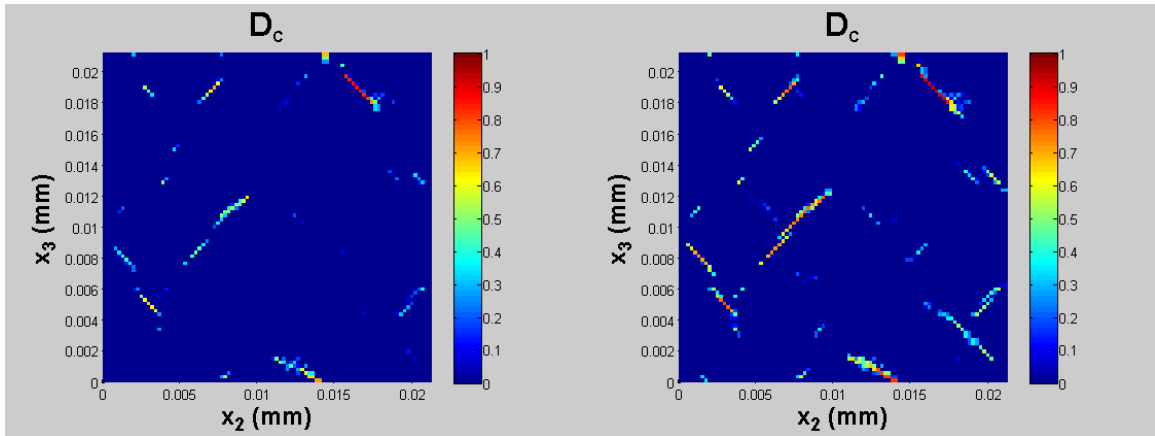
(d) $\epsilon_{22} = -0.00543$, $\sigma_{22} = -87.71$ MPa.



(e) $\epsilon_{22} = -0.00578$, $\sigma_{22} = -92.88$ MPa.

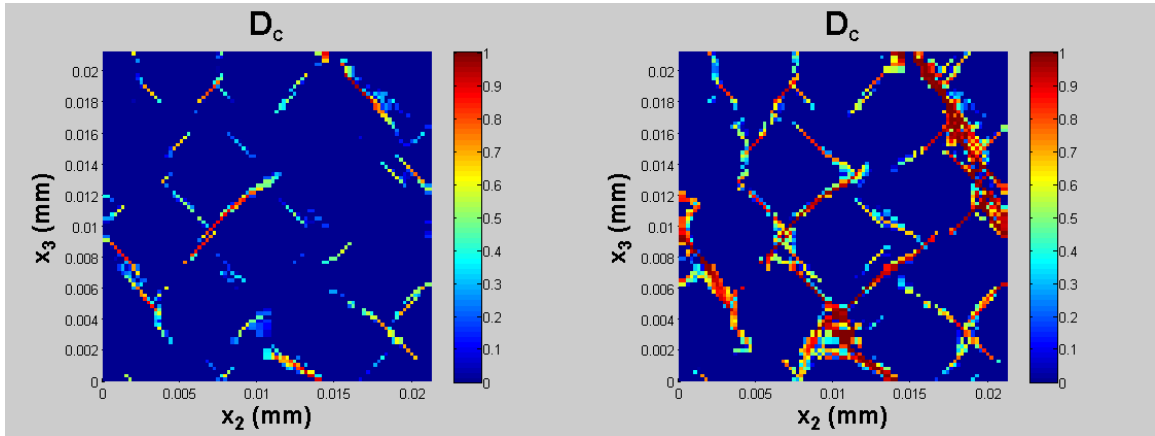
(f) $\epsilon_{22} = -0.00630$, $\sigma_{22} = -100.15$ MPa.

Figure 18: Evolution of mode II crack band in RUC subjected to applied transverse compressive strain if mode I crack band evolution is suppressed.



(g) $\epsilon_{22} = -0.00683$, $\sigma_{22} = -106.75$ MPa.

(h) $\epsilon_{22} = -0.00770$, $\sigma_{22} = -116.36$ MPa.



(i) $\epsilon_{22} = -0.01420$, $\sigma_{22} = -146.43$ MPa (ultimate stress).

(j) $\epsilon_{22} = -0.01750$, $\sigma_{22} = -82.87$ MPa.

Figure 18: Evolution of mode II crack band in RUC subjected to applied transverse compressive strain if mode I crack band evolution is suppressed.

References

- Aboudi, J. (1991), *Mechanics of Composite Materials: A Unified Micromechanical Approach*, Elsevier Amsterdam.
- Aboudi, J. (1995), Micromechanical analysis of thermo-inelastic multiphase short-fiber composites, *Compos. Eng.*, 5(7), 839–850.
- Aboudi, J., M.-J. Pindera, and S. M. Arnold (1999), Higher-order theory for functionally graded materials, *Composites Part B - Engineering*, 30, 777–832.
- Aboudi, J., M.-J. Pindera, and S. M. Arnold (2001), Linear thermoelastic higher-order theory for periodic multiphase materials, *J. Appl. Mech.*, 68, 697–707.
- Aboudi, J., M.-J. Pindera, and S. M. Arnold (2003), Higher-order theory for periodic multiphase materials with inelastic phases, *Int. J. Plast.*, 19, 805–847.
- Aboudi, J., S. M. Arnold, and B. A. Bednarczyk (2012), *Micromechanics of Composite Materials: A Generalized Multiscale Analysis Approach*, Elsevier, in press.
- Aragonés, D. (2007), Fracture micromechanisms in c/epoxy composites under transverse compression, Ph.D. thesis, Universidad Politécnica de Madrid, Madrid, Spain.
- Ashby, M. F., and C. G. Sammis (1990), The damage mechanics of brittle solids in compression, *Pure Appl. Geophys.*, 133(3), 489–520.
- Bansal, Y., and M.-J. Pindera (2004), Testing the predictive capability of the high-fidelity generalized method of cells using an efficient reformulation, *NASA/CR 2004-213043*.
- Bažant, Z., and L. Cedolin (1979), Blunt crack band propagation in finite element analysis, *J. Eng. Mech. Div.-ASCE*, 105, 297–315.
- Bažant, Z. P. (1982), Crack band model for fracture of geomaterials, in *Proceedings of the 4th International Conference on Numerical Methods in Geomechanics*, Edmonton, Canada.
- Bažant, Z. P. (2007), Can multiscale-multiphysics methods predict softening damage and structural failure?, *Mech. Amer. Acad. Mech.*, 36(5-6), 5–12.
- Bažant, Z. P., and L. Cedolin (1983), Finite element modeling of crack band propagation, *J. of Struc. Eng.*, 109, 69–92.
- Bažant, Z. P., and L. Cedolin (1991), *Stability of Structures: Elastic, Inelastic, Fracture and Damage Theories*, Oxford University Press, New York, Oxford.
- Bažant, Z. P., and B. H. Oh (1983), Crack band theory for fracture of concrete, *Mater. and Struct.*, 16, 155–77.

- Bednarczyk, B. A., and S. M. Arnold (2002a), Mac/gmc 4.0 user's manual - keywords manual, *Nasa tm-2002-212077/vol2*.
- Bednarczyk, B. A., and S. M. Arnold (2002b), Mac/gmc 4.0 user's manual - example problems manual, *Nasa tm-2002-212077/vol3*.
- Bednarczyk, B. A., S. M. Arnold, J. Aboudi, and M.-J. Pindera (2004), Local field effects in titanium matrix composites subject to fiber-matrix debonding, *Int. J. Plast.*, *20*, 1707–1737.
- Bednarczyk, B. A., J. Aboudi, and S. M. Arnold (2010), Micromechanics modeling of composites subjected to multiaxial progressive damage in the constituents, *AIAA J.*, *48*, 1367–1378.
- Camanho, P. P., P. Maimí, and C. G. Dávila (2007), Prediction of size effects in notched laminates using continuum damage mechanics, *Compos. Sci. and Technol.*, *67*, 2715–2727.
- Chen, W., and G. Ravichandran (2000), Failure mode transition in ceramics under dynamic multiaxial compression, *Int. J. Fract.*, *101*, 141–159.
- de Borst, R., and P. Nauta (1985), Non-orthogonal cracks in a smeared finite element model, *Eng. Comput.*, *2*, 35–46.
- deBorst, R. (1987), Computation of post-bifurcation and post-failure behavior of strain-softening solids, *Comput. Struct.*, *25*, 211–224.
- Gamstedt, E. K., and B. A. Sjögren (1999), Micromechanisms in tension-compression fatigue of composite laminates containing transverse plies, *Compos. Sci. Technol.*, *59*, 167–178.
- Gonzaléz, C., and J. Llorca (2007), Mechanical behavior of unidirectional fiber-reinforced polymers under transverse compression: Microscopic mechanisms and modeling, *Compos. Sci. Technol.*, *67*, 2795–2806.
- Haj-Ali, R., and J. Aboudi (2009), Nonlinear micromechanical formulation of the high fidelity generalized method of cells, *Int. J. Solids Struct.*, *46*, 2577–2592.
- Haj-Ali, R., and J. Aboudi (2010), Formulation of the high-fidelity generalized method of cells with arbitrary cell geometry for refined micromechanics and damage in composites, *Int. J. Solids Struct.*, *47*, 3447–3461.
- Hinton, M. J., A. S. Kaddour, and P. D. Soden (Eds.) (2004), Elsevier, New York.
- Hoek, E., and Z. T. Bieniawski (1965), Brittle rock fracture propagation in rock under compression, *Int. J. Fract.*, *1*(3), 137–155.
- Horii, H., and S. Nemat-Nasser (1986), Brittle failure in compression: Splitting, faulting and brittle-ductile transition, *Philos. T. R. Soc. S.-A.*, *319*(1549), 337–374.

- Ng, W. H., A. G. Salvi, and A. M. Waas (2010), Characterization of the in-situ non-linear shear response of laminated fiber-reinforced composites, *Compos. Sci. Technol.*, 70(7), 1126–1134.
- Paley, M., and J. Aboudi (1992), Micromechanical analysis of composites by the generalized cells model, *Mechanics of Materials*, 14, 127–139.
- Pietruszczak, S., and Z. Mroz (1981), Finite element analysis of deformation of strain-softening materials, *Int. J. Numer. Methods Eng.*, 17, 327–334.
- Pindera, M. J., and B. A. Bednarczyk (1997), An efficient implementation of the gmc micromechanics model for multi-phased materials with complex microstructures, *NASA/CR 1997-202350*.
- Pineda, E. J., A. M. Waas, B. A. Bednarczyk, and C. S. Collier (2010a), An efficient semi-analytical framework for micromechanical modeling of transverse cracks in fiber-reinforced composites, in *51st AIAA/ASME/ASCE/AHS/ASC Structures, Structural Dynamics, and Materials Conference*.
- Pineda, E. J., A. M. Waas, B. A. Bednarczyk, and C. S. Collier (2010b), Multiscale modeling of progressive microdamage and transverse cracking in fiber reinforced laminates, in *Presented at the 16th US National Conference of Theoretical and Applied Mechanics*.
- Pinho, S. T., C. G. Dávila, P. P. Camanho, and L. Iannucci (2005), Failure models and criteria for frp under in-plane or three-dimensional stress states including shear non-linearity, *NASA/TM 2005-213530*.
- Puck, A., and H. Schürmann (1998), Failure analysis of frp laminates by means of physically based phenomenological models, *Compos. Sci. Technol.*, 58, 1045–1067.
- Puck, A., and H. Schürmann (2002), Failure analysis of frp laminates by means of physically based phenomenological models, *Compos. Sci. Technol.*, 62, 1633–1622.
- Roberts, S. J. (2000), Modelling of microcracking in composite materials, Ph.D. thesis, The University of Newcastle upon Tyne, Newcastle upon Tyne, United Kingdom.
- Rots, J. G., and R. de Borst (1987), Analysis of mixed-mode fracture in concrete, *J. Eng. Mech.*, 113(11), 1739–1758.
- Spencer, B. W. (2002), Finite elements with embedded discontinuities for modeling reinforced concrete members, Ph.D. thesis, Brigham Young University, Provo, UT.
- Taliercio, A., and P. Sagramoso (1995), Uniaxial strength of polymeric-matrix fibrous composites predicted through a homogenization approach, *Int. J. Solids Struct.*, 32(14), 2095–2123.

REPORT DOCUMENTATION PAGE			Form Approved OMB No. 0704-0188		
<p>The public reporting burden for this collection of information is estimated to average 1 hour per response, including the time for reviewing instructions, searching existing data sources, gathering and maintaining the data needed, and completing and reviewing the collection of information. Send comments regarding this burden estimate or any other aspect of this collection of information, including suggestions for reducing this burden, to Department of Defense, Washington Headquarters Services, Directorate for Information Operations and Reports (0704-0188), 1215 Jefferson Davis Highway, Suite 1204, Arlington, VA 22202-4302. Respondents should be aware that notwithstanding any other provision of law, no person shall be subject to any penalty for failing to comply with a collection of information if it does not display a currently valid OMB control number.</p> <p>PLEASE DO NOT RETURN YOUR FORM TO THE ABOVE ADDRESS.</p>					
1. REPORT DATE (DD-MM-YYYY) 01-06-2012		2. REPORT TYPE Technical Memorandum		3. DATES COVERED (From - To)	
4. TITLE AND SUBTITLE Implementation of a Smeared Crack Band Model in a Micromechanics Framework			5a. CONTRACT NUMBER		
			5b. GRANT NUMBER		
			5c. PROGRAM ELEMENT NUMBER		
6. AUTHOR(S) Pineda, Evan, J.; Bednarczyk, Brett, A.; Waas, Anthony, M.; Arnold, Steven, M.			5d. PROJECT NUMBER		
			5e. TASK NUMBER		
			5f. WORK UNIT NUMBER WBS 984754.02.07.03.16.03.02		
7. PERFORMING ORGANIZATION NAME(S) AND ADDRESS(ES) National Aeronautics and Space Administration John H. Glenn Research Center at Lewis Field Cleveland, Ohio 44135-3191			8. PERFORMING ORGANIZATION REPORT NUMBER E-18184		
9. SPONSORING/MONITORING AGENCY NAME(S) AND ADDRESS(ES) National Aeronautics and Space Administration Washington, DC 20546-0001			10. SPONSORING/MONITOR'S ACRONYM(S) NASA		
			11. SPONSORING/MONITORING REPORT NUMBER NASA/TM-2012-217603		
12. DISTRIBUTION/AVAILABILITY STATEMENT Unclassified-Unlimited Subject Categories: 24, 39, and 61 Available electronically at http://www.sti.nasa.gov This publication is available from the NASA Center for AeroSpace Information, 443-757-5802					
13. SUPPLEMENTARY NOTES					
14. ABSTRACT The smeared crack band theory is implemented within the generalized method of cells and high-fidelity generalized method of cells micromechanics models to capture progressive failure within the constituents of a composite material while retaining objectivity with respect to the size of the discretization elements used in the model. An repeating unit cell containing 13 randomly arranged fibers is modeled and subjected to a combination of transverse tension/compression and transverse shear loading. The implementation is verified against experimental data (where available), and an equivalent finite element model utilizing the same implementation of the crack band theory. To evaluate the performance of the crack band theory within a repeating unit cell that is more amenable to a multiscale implementation, a single fiber is modeled with generalized method of cells and high-fidelity generalized method of cells using a relatively coarse subcell mesh which is subjected to the same loading scenarios as the multiple fiber repeating unit cell. The generalized method of cells and high-fidelity generalized method of cells models are validated against a very refined finite element model.					
15. SUBJECT TERMS Fiber composites; Polymer matrix composites; Carbon fiber reinforced plastics; Computational mechanics; Damage; Fracture mechanics; Micromechanics					
16. SECURITY CLASSIFICATION OF:			17. LIMITATION OF ABSTRACT	18. NUMBER OF PAGES	19a. NAME OF RESPONSIBLE PERSON
a. REPORT	b. ABSTRACT	c. THIS PAGE			STI Help Desk (email:help@sti.nasa.gov)
U	U	U	UU	58	19b. TELEPHONE NUMBER (include area code) 443-757-5802

